8-2022

Kinematic and Vorticity Analysis of the Slide Lake and Homestake Shear Zones, Central Colorado

Carsen T. Adams
University of Tennessee, Knoxville, cadams58@vols.utk.edu

To the Graduate Council:

I am submitting herewith a thesis written by Carsen T. Adams entitled "Kinematic and Vorticity Analysis of the Slide Lake and Homestake Shear Zones, Central Colorado." I have examined the final electronic copy of this thesis for form and content and recommend that it be accepted in partial fulfillment of the requirements for the degree of Master of Science, with a major in Geology.

Micah J. Jessup, Major Professor

We have read this thesis and recommend its acceptance:

Robert D. Hatcher, Nicholas J. Dygert, Bradley J. Thomson

Accepted for the Council:
Dixie L. Thompson

Vice Provost and Dean of the Graduate School

(Original signatures are on file with official student records.)

KINEMATIC AND VORTICITY ANALYSIS OF THE SLIDE LAKE AND HOMESTAKE SHEAR ZONES, CENTRAL COLORADO

A Thesis Presented for the
Master of Science
Degree
The University of Tennessee, Knoxville

Carsen Thomas Adams
August 2022

ACKNOWLEDGEMENTS

A sincere thank you is owed to all of those who helped me with this project, and to those who helped me become a better student and person. I could not have made it through this project without help. I would like to thank my advisor, Micah Jessup, for his patience and guidance during my progression as a researcher. I thank my committee members, Dr. Robert Hatcher, Dr. Nick Dygert, and Dr. Bradley Thomson, for providing guidance and mentorship throughout my time at UTK. I thank the Tobacco Root Geological Society for funding through a field scholarship. I would also like to thank Dr. Joseph Allen for his hospitality while in Leadville, CO. Thanks also to Dr. Colin Shaw at Montana State University for EBSD collection and valuable insight. Many thanks to my lab group members, Tyler Grambling and Corey Flynn, for providing invaluable help, guidance, and positivity whenever I needed it the most.

Thank you to my countless friends, near and far, who helped me stay positive and for giving me some good laughs along the way. You all have changed my life for the better. Thank you to Hannah, Sydney, and Nick for helping me explore Knoxville and try new things. Thank you to Jake for being a great friend. Your thoughtful advice and ability to listen is a gift. Thank you to my office mates, Chance, Constance, and Julie for making me always feel at home. I would like to thank all of my fellow graduate students for their support throughout the past two years, specifically Allison, Morgan, Jesse, Brianna, Micki, Ivy, Sara, Cat, and Helle. In addition, I would like to thank my parents and grandparents for their unwavering support and advice.

ABSTRACT

Kinematic and quantitative vorticity analysis of the Homestake shear zone (HSZ) and the Slide Lake shear zone (SLSZ) in central Colorado provide insight into crustal processes that controlled deformation within the Colorado Mineral Belt (CMB) shear zone system throughout the Proterozoic. Evaluating vorticity, that is, the relative contributions of pure to simple shear in sheared rocks, is crucial to understanding lithospheric tectonic evolution and allows for kinematic modeling of shear zone development at a variety of scales. Moreover, novel vorticity analyses involve determining the orientation of the vorticity vector and vorticity normal surface which can give insight into shear zone geometry independent of fabric elements. The CMB is a system of Laramide age plutons that lie within a Proterozoic zone of weakness defined by northeast-striking shear zones that have been repeatedly activated since ~1.7 Ga. The steeply dipping HSZ consists of a set of anastomosing shear stands that outcrop as mylonite and ultramylonite zones in Homestake valley. The SLSZ outcrops as three gently dipping mylonite zones with variable thickness above tree line on Homestake peak. Kinematic indicators within mylonite from the HSZ and SLSZ record top-down-to-the-southeast, top-up-to-the-northeast, and dextral movement suggesting the shear zones are kinematically linked and were active at similar mid-crustal levels (Lee et al., 2012). Further detailed microstructural analysis and crystallographic vorticity axis analysis, utilizing newly acquired electron backscatter diffraction data, were implemented on all phases to produce the orientation of the bulk vorticity vector and vorticity normal surface in the HSZ and SLSZ. We apply these results to reevaluate the model of shear zone

deformation proposed by previous research. Additionally, quartz slip system analysis was conducted on samples from the field area to estimate temperatures associated with mylonite development. We conclude that strain localization within the HSZ involved general shear within a monoclinic, wrench-dominated transpressional setting. Results from this analysis demonstrate that the SLSZ likely exhibits a triclinic component of deformation. This research demonstrates the utility of modern vorticity analysis as applied to mono- and polyphase lithologies.

TABLE OF CONTENTS

CHAPTER 1: INTRODUCTION **1**
CHAPTER 2: BACKGROUND **9**
2.1 Tectonic Setting **10**
2.2 Geology of the Colorado Mineral Belt **11**
2.3 The Homestake shear zone **16**
2.4 The Slide Lake shear zone **19**
2.5 Kinematic framework **25**
CHAPTER 3: METHODS **30**
3.1 Field Visit and Mesoscale Observations **30**
3.2 Thin Sections and Petrography **31**
3.3 Electron Backscatter Diffraction **32**
3.4 Slip System Analysis **33**
3.5 Crystallographic Vorticity Axis Analysis **34**
3.6 FABRICA Analysis **38**
CHAPTER 4: RESULTS **40**
4.1 Petrography and Sample Descriptions **40**
4.2 Slip-System Analysis and Deformation Temperature Estimates **49**
4.3 Crystallographic vorticity axis analysis **54**
4.4 FABRICA Analysis **57**
CHAPTER 5: DISCUSSION **61**
5.1 Deformation Temperatures and Quartz Crystallographic Preferred Orientation Plots **61**
5.2 Crystallographic Vorticity Axis Analysis **63**
5.3 Low-Angle Intragranular Boundary Misorientations **66**
CHAPTER 6: CONCLUSION **68**
CHAPTER 7: FUTURE WORK **70**
REFERENCES **71**
APPENDICES **78**
APPENDIX I: MATLAB Scripts **78**

APPENDIX II: Sample Data.....82
VITA.....85

LIST OF TABLES

Table 1: Summary of deformation conditions for the Homestake shear zone. 13

Table 2: Summary of Microstructural Analysis.....42

LIST OF FIGURES

Figure 1: Block models depicting the vorticity vector (w) and its relation to the vorticity profile plane and the ISAs.....3
Figure 2: Relationships between vorticity vector, fabric orientations, and shear sense indicators within various types of shear zones. 5
Figure 3: Tectonostratigraphic map of the SW U.S and field area.....6
Figure 4: Location map of the Colorado Mineral Belt (CMB) and Precambrian outcrops in Colorado.....12
Figure 5: Generalized geologic map of the Homestake shear zone (HSZ) and the Slide Lake shear zone (SLSZ).....14
Figure 6: Geologic cross section of A'-A from Figure 5.....15
Figure 7: Characteristic mesoscale features of the HSZ.....17
Figure 8: Microstructural observations of rocks from the HSZ.....20
Figure 9: Field images and observations of the SLSZ.....23
Figure 10: Microstructural observations from the SLSZ.....24
Figure 11: Schematic block diagram illustrating the kinematic model for HSZ and SLSZ 27
Figure 12: Quartz crystallographic preferred orientation (CPO) dependence on slip system activity and EBSD generated pole figures for the study area 29
Figure 13: Plot showing the relationship between low-angle boundary orientations and slip system activity in quartz.....35
Figure 14: Crystallographic analysis method. 37
Figure 15: Sample HS08-12 photomicrographs, XPL.....43
Figure 16: Sample HS08-13 photomicrographs 44
Figure 17: Sample SL08-04 photomicrographs 45
Figure 18: Photomicrographs of sample HS09-21.....47
Figure 19: Photomicrographs of sample HS09-23. 48
Figure 20: Sample HS09-29 photomicrographs. 50
Figure 21: Lower hemisphere equal area pole figures of Quartz c- and a-axis 52

Figure 22: Wedge plots showing the results of quartz low-angle, intragranular boundary misorientation analysis.....55
Figure 23: Lower hemisphere, equal area stereonets showing the orientation of the bulk vorticity axis.....58
Figure 24: Lower hemisphere, equal area projections showing phase specific crystallographic vorticity axis.....59
Figure 25: Rotated CVA plots shown in the geographic reference frame using fabric foliation and stretching lineation orientations.....60

CHAPTER 1: INTRODUCTION

Strain accumulation in the lithosphere often localizes into tabular zones known as shear zones that can vary from micro-scale zones to regional structures that can be several kilometers in width. Moreover, such zones can exhibit a large degree of heterogeneity, showing large variations in orientation, displacement, strain geometry, coaxiality, and deformation mechanisms (Fossen & Cavalcante, 2017). Contrary to the initial models of shear zone development, which strictly involved simple shear (Ramsay & Graham, 1970), it is now accepted that high strain zones involve components of simple and pure shear, suggesting it is more appropriate to interpret these zones based on the degree of non-coaxiality as opposed to either perfectly non-coaxial or coaxial flow (Law et al., 1984, 1986; Platt & Behrmann 1986; Xypolias, 2010). Understanding the degree of non-coaxiality in a deformed region can be achieved by determining the kinematic vorticity number (W_k) (Truesdell 1953; Means et al., 1980).

Understanding the kinematics of flow in shear zones has been crucial to the understanding of lithospheric tectonic evolution, as well as interpreting the structural significance of fabrics in deformed rocks. Vorticity is a measure of rotation relative to the amount of stretching (Tikoff & Fossen, 1995). In a geologic context, vorticity is a measurement of the relative amounts of pure and simple shear and can be used to quantify kinematic flow in deformed rocks (Xypolias, 2010; Fossen & Cavalcante, 2017). The kinematic vorticity number is used to describe intermediate contributions of pure shear (Wk = 0) and simple shear (Wk = 1), where a Wk of 0.71 represents equal contributions of both (Tikoff & Fossen, 1995). In certain cases, vorticity is more

appropriately described with the mean kinematic vorticity number (W_m), which represents a time averaged quantity of W_k. Since its introduction into geologic literature by Means et al. (1980), methods for vorticity analysis have become increasingly sophisticated (Passchier and Urai, 1988; Wallis, 1992; Tikoff and Fossen, 1995; Simpson and De Paor, 1997; Jessup et al., 2007). However, traditional vorticity models heavily rely on assumptions about the orientation of rigid particles and the orientation of the vorticity normal plane, which does not always correspond to the common kinematic reference frame (XZ plane of the finite strain ellipsoid, i.e., orthogonal to the foliation plane, parallel to the stretching lineation) (Xypolias, 2010; Diaz-Azpiroz et al., 2018; Kruckenberg et al., 2019).

The vorticity vector lies parallel to the pole to the vorticity normal-plane and represents the axis around which rotation and stretching is the greatest (Robin and Cruden, 1994; Tikoff and Fossen, 1995; Xypolias, 2010). The geometry of a deforming zone can be determined by evaluating the orientation of the vorticity vector relative to flow parameters and accumulation of finite strain. Throughout deformation, the orientation of maximum and minimum stretching can be described by three orthogonal axes known as instantaneous stretching axes (ISA's) (Passchier, 1998). A shear zone is said to have a monoclinic geometry if the vorticity vector is parallel with one of the ISA's (Figure 1a). A triclinic shear zone is described as having a vorticity vector that is oblique to one of the ISAs (Figure 1b). It is important that kinematic interpretations are determined in the vorticity profile plane (i.e., vorticity normal plane), which is often assumed to correspond to the plane parallel to lineation and perpendicular to foliation

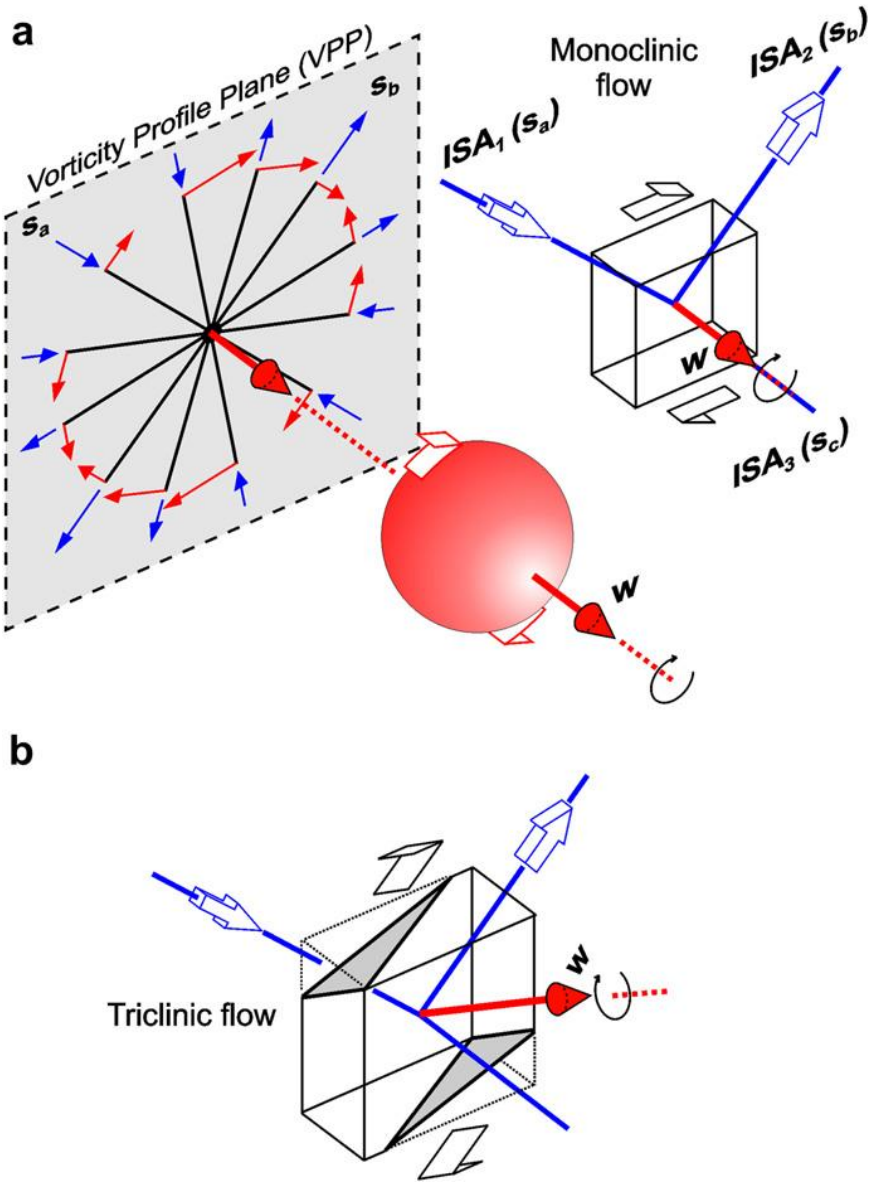

Figure 1: Block models depicting the vorticity vector (w) and its relation to the vorticity profile plane and the ISAs. (a.) Block model depicting a monoclinic flow geometry. The vorticity vector (w) is parallel with one of the ISAs. (b.) Block model depicting a triclinic flow geometry with w oblique to all three ISAs (Xypolias, 2010).

(i.e., the XZ plane of the finite strain ellipsoid and monoclinic; Fig 2A) however this is not always true. The vorticity vector can be oriented parallel (e.g., monoclinic transpression; Figure 2B), perpendicular (e.g., monoclinic simple shear; Figure 2A), or oblique (e.g., triclinic; Figure 2D) to the stretching lineation direction (Figure 2D). Therefore, accurately identifying the vorticity normal plane is crucial to modern vorticity analysis of shear zones. Specifically, the determination of the orientation of the vorticity vector can be used to evaluate the accuracy of kinematic interpretations, determine the geometry of the deforming zone, establish a common geographic reference frame, and reconstruct paleoconvergence vectors. This project will focus on applying a modern vorticity analysis technique, known as crystallographic vorticity axis (CVA) analysis (Michels et al., 2015), to the Homestake and Slide Lake shear zones within the Colorado Mineral Belt (CMB) in central Colorado in order to identify the orientation of the bulk vorticity axis and vorticity normal surface.

The Colorado Mineral Belt (CMB) is a northeast-striking long-lived tectonic zone in the southern Rocky Mountains. The CMB is well known for its suite of Laramide-aged (77–55 Ma) plutons and ore deposits that likely are the product of magma emplacement that was localized due to crustal weakening associated with Proterozoic accretion along the western Laurentian margin. Proterozoic deformation localized into shear zones that strike northeast across the central portion of Colorado (Figure 3). Kinematics and timing of deformation of shear zones in the CMB are generally well understood (Tweto and Sims, 1963; Karlstrom and Bowring, 1988; Bowring and Karlstrom, 1990; Shaw and Karlstrom, 1999; Shaw et al., 2001; McCoy et al., 2005; Lee et al., 2012). The

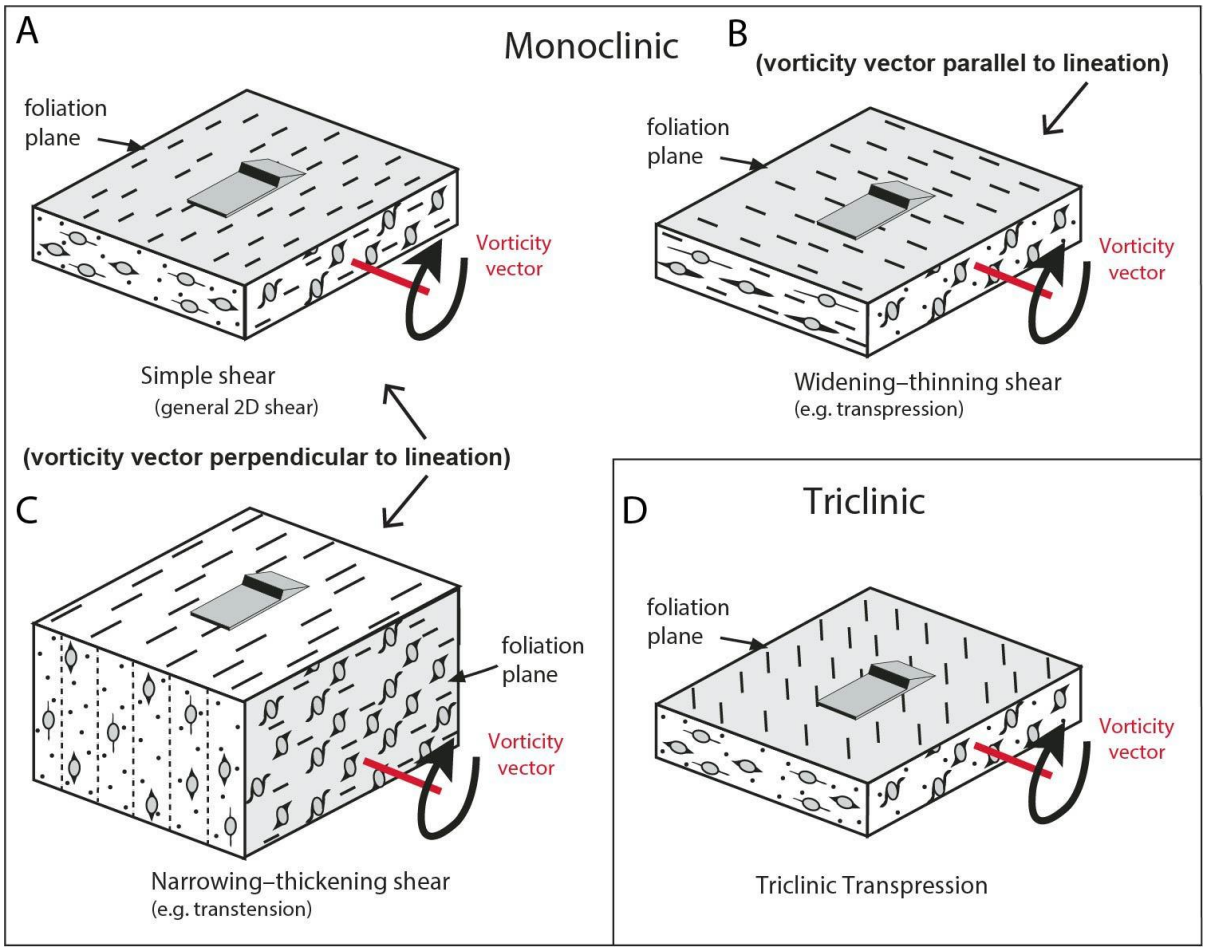

Figure 2: Relationships between vorticity vector, fabric orientations, and shear sense indicators within various types of shear zones. Modified from Tikoff et al., 2013; Michels et al., 2015.

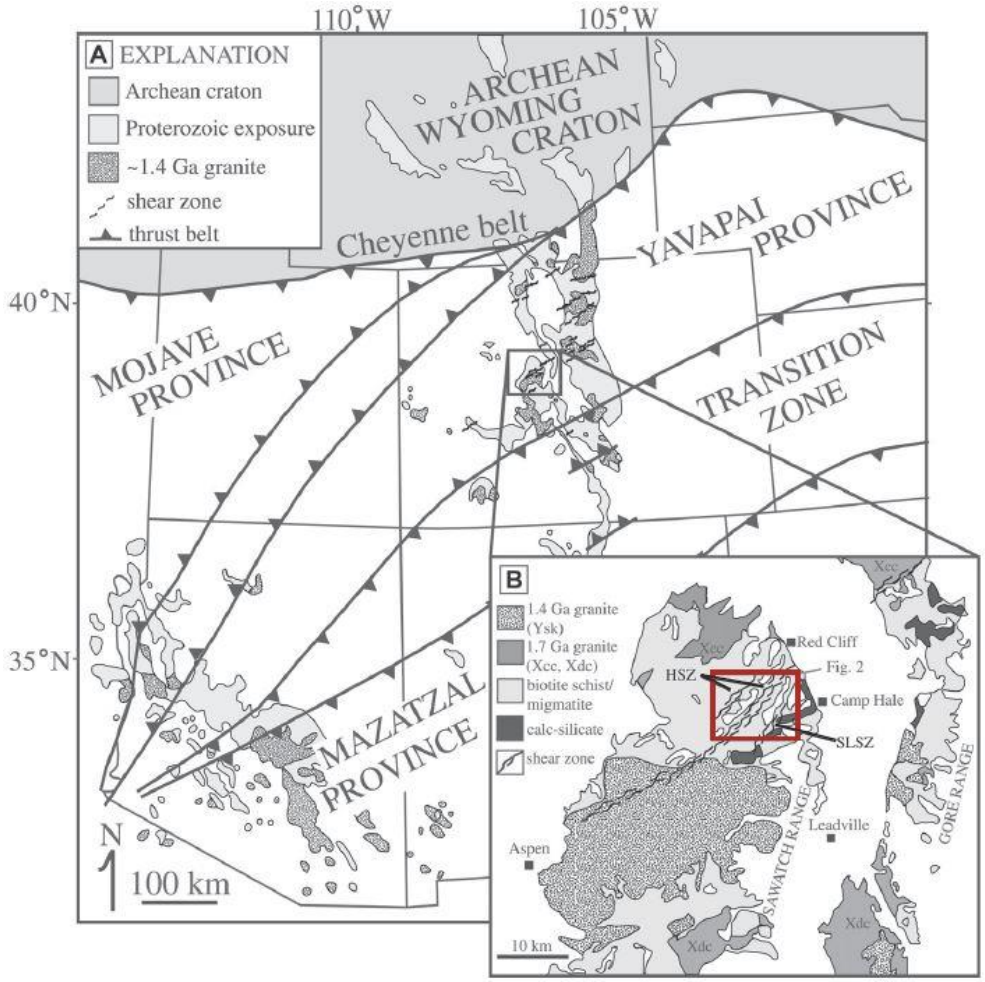

Figure 3: Tectonostratigraphic map of the SW U.S and field area. A) Regional map of Proterozoic, tectonic assembly in the southwestern U.S. (Condie, 1986; Bennett and Depaolo, 1987; Karlstrom and Bowring, 1988; Wooden et al., 1988; Wooden and DeWitt, 1991; Jones et al., 2010; Lee et al., 2012). B) Generalized geologic map of the Homestake shear zone (HSZ) and the Slide Lake shear zone (SLSZ) in central Colorado. Red box depicts approximate field area (Tweto, 1979; Shaw and Allen, 2007; modified from Lee et al., 2012).

development of 1.4 Ga shear zones and younger magmatism are thought to be a response to far-field shortening between southern Laurentia and another piece of continental crust (Nyman et al., 1994; Duebendorfer and Christensen, 1995; Karlstrom and Humphreys, 1998; McCoy et. al., 2005; Jones et al., 2010a; Lee et al., 2012). Within the CMB, the Homestake and Slide Lake shear zones (HSZ and SLSZ, respectively) offer a spectacular natural laboratory for modern vorticity analysis that provide important information about kinematic processes. The rocks in these shear zones record multiple stages of deformation, displaying deformation fabrics and recrystallization mechanisms at a variety of scales, that represent a manifestation of mid-crustal shortening related to Laurentian continental evolution.

The HSZ and SLSZ consist of mylonite, ultramylonite, and pseudotachylyte zones that cut across a complex assortment of high-temperature, variably folded migmatite, schist, calc-silicate schist, and amphibolite (Tweto, 1974; Shaw et al., 2001). Meso- and microscale kinematic observations, fabric relationships, and radiometric dating estimates from rocks in the HSZ and SLSZ suggest that the two are kinematically and temporally linked, both containing mylonite that record top-down-to-the southeast, top-up-to-the northwest, and dextral movement (Lee et al., 2012). This contribution will employ a relatively novel method of kinematic vorticity analysis known as crystallographic vorticity axis (CVA) analysis (Michels et al., 2015) to determine the orientation of the bulk vorticity axis of sheared rocks and independently test previous kinematic and deformation models for the HSZ and SLSZ (Lee et al., 2012).

The steeply dipping, northeast striking HSZ cross cuts the Proterozoic crystalline basement rock of the northern Sawatch Range north of Leadville, Colorado. The HSZ was initially mapped as an anastomosing system of cataclastic gneiss zones (Tweto, 1974). Subsequent mapping has revealed that the HSZ is a composite result of distinguishable deformation events that occurred between 1.7-1.4 Ga that initiated as a mylonitic, gneissic, high strain zone that was overprinted by mylonite/ultramylonite zones and pseudotachylyte development (Shaw, 2001; Allen et al., 2002; Allen, 2005; Lee et al., 2012). The less-studied SLSZ dips gently to the southeast and crosscuts variable gneiss and migmatite that also exhibits mylonite/ultramylonite zones and pseudotachylyte and is interpreted to be contemporaneous with deformation in the HSZ (Lee et al., 2012).

CHAPTER 2: BACKGROUND

Typical models of continental growth involve pulses of active tectonism whereby crust is added onto existing continental crust via an active margin, resulting in rocks that exhibit brittle and ductile structures associated with shortening, elongation, and shearing. Through recurrent continental growth, these structures can develop into intracontinental zones of weakness that lead to further reactivation and can potentially localize magma and ore bodies (Hamilton, 1981; Molnar, 1988; Bowring and Karlstrom, 1990; Teyssier et al., 1995; Lee et al., 2012). The southern Rocky Mountain region records the assembly, stabilization, and early phases of degradation of the North American continent; thus, it is one of the finest places in the world to study continental evolution. Several decades of research have helped constrain the history of shear zone activity in central Colorado (Tweto and Sims, 1963; Tweto, 1974; Shaw et al., 2001; McCoy et al., 2005; Jessup et al., 2005; Shaw and Allen, 2007; Lee et al., 2012). The crystalline core of the Rocky Mountains is remarkable because much of the Proterozoic (2.5–0.54 Ga) bedrock is well preserved despite Cenozoic (66 Ma to present) modification and overprinting, suggesting older lithospheric structures have controlled younger tectonic and magmatic activity (Karlstrom and Keller, 2005). Accretion of continental lithosphere along the southwestern margin of Laurentia during the Proterozoic involved several episodes of active tectonism and northeastern convergence of arc terranes (Whitmeyer and Karlstrom, 2007; Lee et al., 2012), resulting in a series of northeast-striking shear zones that record various stages of deformation associated with the Proterozoic formation of North America and subsequent magmatism and subsequent exposure on the surface

(Tweto and Sims, 1963; Bowring and Karlstrom, 1990; Nyman et al., 1994; Karlstrom and Humphreys, 1998; Shaw et al., 2001; Lee et al., 2012). Based on distinct compositional and geochronologic terranes, the Proterozoic accretionary belt can be divided into three dominant crustal provincesthat extend from southern Wyoming southward to New Mexico: the Mazatzal, Yavapai, and Mojave (Figure 3A; Karlstrom and Houston, 1984; Duebendorfer et al., 1987; Karlstrom and Bowring, 1988; Bowring and Karlstrom, 1990; Bickford and Hill, 2007).

2.1 Tectonic Setting

Laurentia, the North American craton, was assembled from several Archean crustal blocks during a period of Paleoproterozoic orogenesis known as the Trans-Hudson orogeny (Hoffman, 1988; Whitmeyer and Karlstrom, 2007; Darbyshire et al., 2017). This orogeny involved the Laurentian margin along which juvenile crust accumulated due to the amalgamation of arc terranes throughout the Proterozoic. The oldest phase of deformation is recorded by the assembly of the Yavapai province (1.78 to 1.70 Ga) consisting of arc-derived rocks and blocks of older continental crust, across a system of northeast- northwest-striking subduction zones (Duebendorfer et al., 1987, Shaw and Karlstrom, 1999; Hill and Bickford, 2001; Jessup et al., 2005, 2006). Subsequent deformation involved the addition of the Mazatzal province (1.68 to 1.65 Ga), a package of tectonostratigraphic arc terranes, along a northeast-striking convergent boundary (Karlstrom and Bowring, 1988; Shaw and Karlstrom, 1999). Following the assembly of the Mazatzal province, a ~200 m.y. period of tectonic stability persisted until 1.4 Ga when granitoid intrusion began accompanied by northwest-oriented shortening

and strike-slip movement until approximately 1.36 Ga (Karlstrom and Bowring, 1988; Nyman et al, 1994; Shaw et al., 2001; Jessup et al., 2005, 2006). The onset of the Laramide orogeny occurred during the Late Cretaceous (Hoffman, 1988).

2.2 Geology of the Colorado Mineral Belt

The Colorado Mineral belt (CMB) is a northeast-striking, long-lived tectonic zone in the southern Rocky Mountains that outcrops west of Boulder, CO and extends to the southwest (Figure 4). The CMB hosts a complex suite of Laramide-age plutons and ore deposits that likely resulted from magma emplacement that was localized due to inherited zones of crustal weakness formed throughout accretion along the Laurentian margin during the Proterozoic. The kinematics and timing of deformation in shear zones within the CMB are well constrained (e.g., Figure 4, Table 1; Tweto and Sims, 1963; Karlstrom and Bowring, 1988; Shaw and Karlstrom, 1999; Shaw et al., 2001; McCoy et al., 2005; Lee et al., 2012). Shear zones within the CMB are typically anastomosing, containing multiple shear splays over a ~1–km wide area. CMB shear zones generally strike northeast (028°–090°; McCoy et al., 2005), predominantly dip sub-vertically (74°NW to 66°SE; McCoy et al., 2005), contain steeply plunging lineations, and are subparallel to high-strain axial-planar cleavage (Shaw et al., 2001; McCoy et al., 2005). Within the central portion of the CMB, the HSZ and SLSZ consist of mylonite, ultramylonite, and pseudotachylyte zones that cut across a complex package of Proterozoic crystalline basement rock (Figure 5 and Figure 6; Tweto, 1974; Shaw et al., 2001). Meso- and microscale kinematic observations, fabric relationships, and radiometric dating estimates from rocks in the HSZ and SLSZ suggest that the two are kinematically and temporally

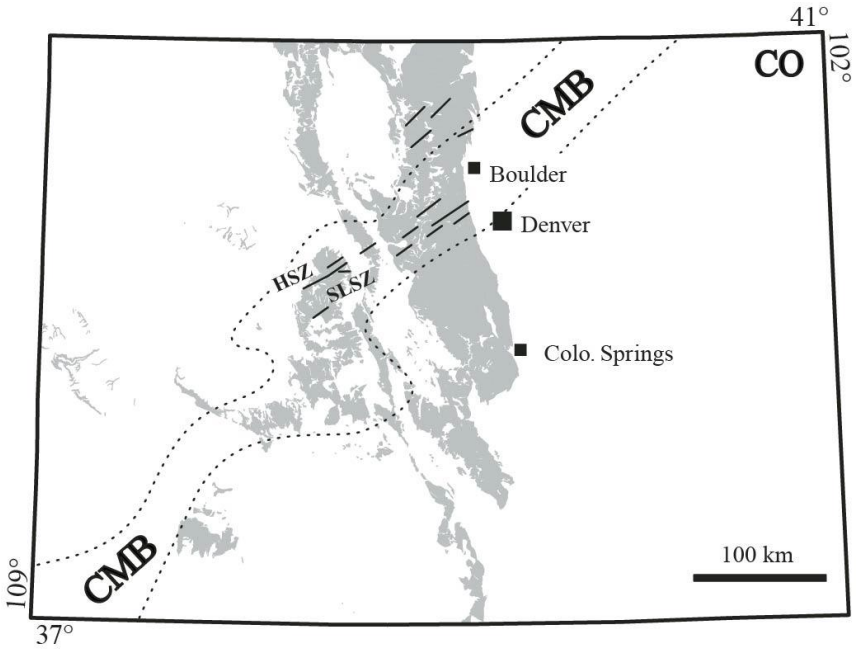

Figure 4: Location map of the Colorado Mineral Belt (CMB) and Precambrian outcrops in Colorado. Black lines indicate Proterozoic shear zones. Approximate locations of the HSZ and SLSZ are noted. Modified from Shaw and Allen, (2013); McCoy et al. (2005).

Table 1: Summary of deformation conditions for the Homestake shear zone.

Event*	***Timing (Ga)***	***Temperature***	***Structure***	***Shear sense***
D_1	> 1.71	High (>500°C)	S_1 sub-horizontal flow, F_1 isoclinal recumbent folds	-
D_2	1.71 – 1.62	High (>500°C)	S_2/F_2 NE-SW trending upright folds	t-NW
D_3	1.42 – 1.38	Moderate (300-500°C)	S_3 subvertical mylonite shear zones	t-SE, dextral
D_4	~ 1.38	Moderate (250-450°C)	S_4 subvertical ultramylonite and pseudotachylyte	t-NW, dextral

*Terminology from Shaw et al., (2001)

Age, temperatures, and shear sense from Shaw et al., (2001); Shaw et al., (2005); Lee et al. (2012)

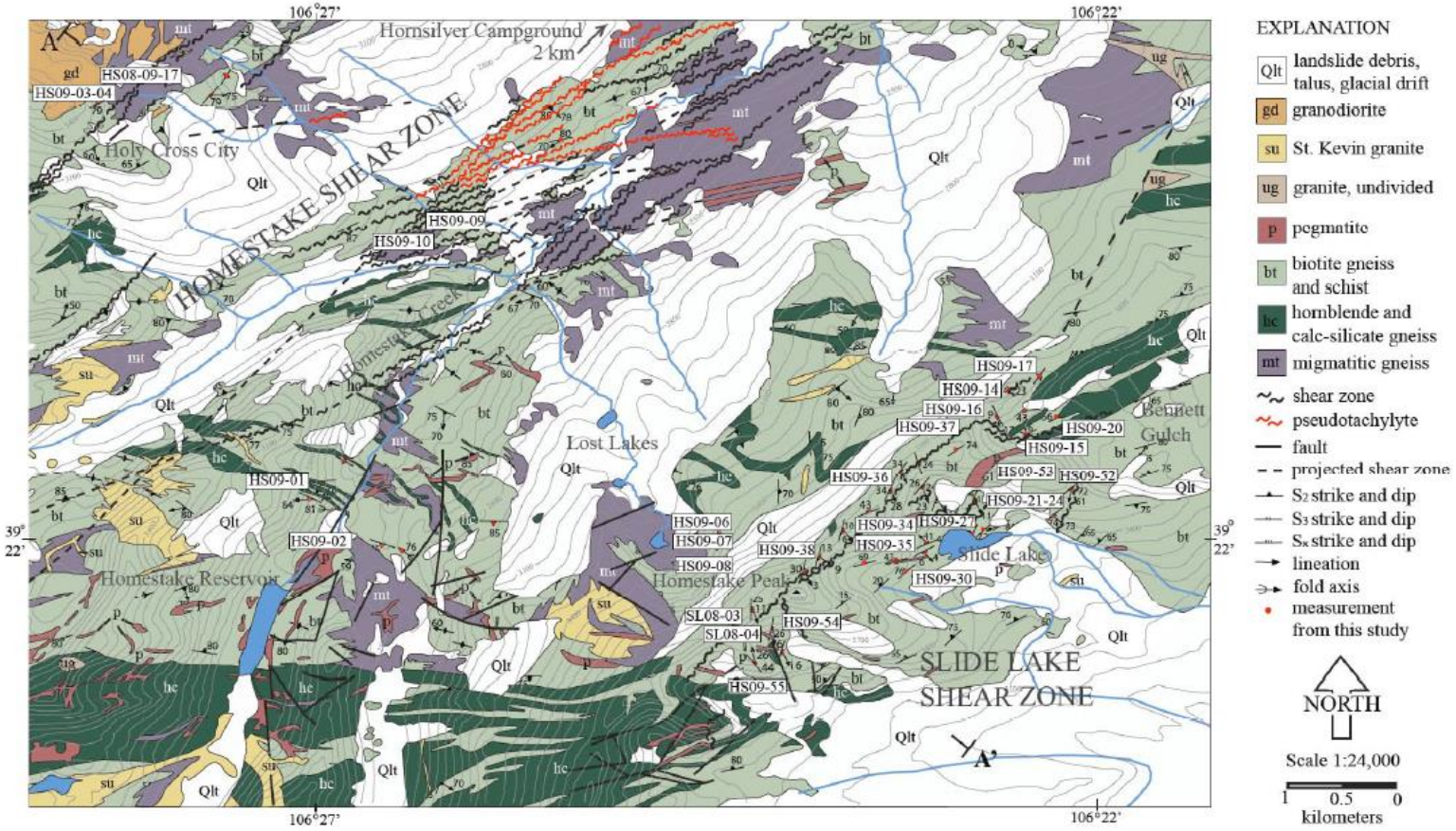

Figure 5: Generalized geologic map of the Homestake shear zone (HSZ) and the Slide Lake shear zone (SLSZ). Sample locations are indicated with white rectangles. Cross-section line A-A' indicated on map. From Lee et al. (2012).

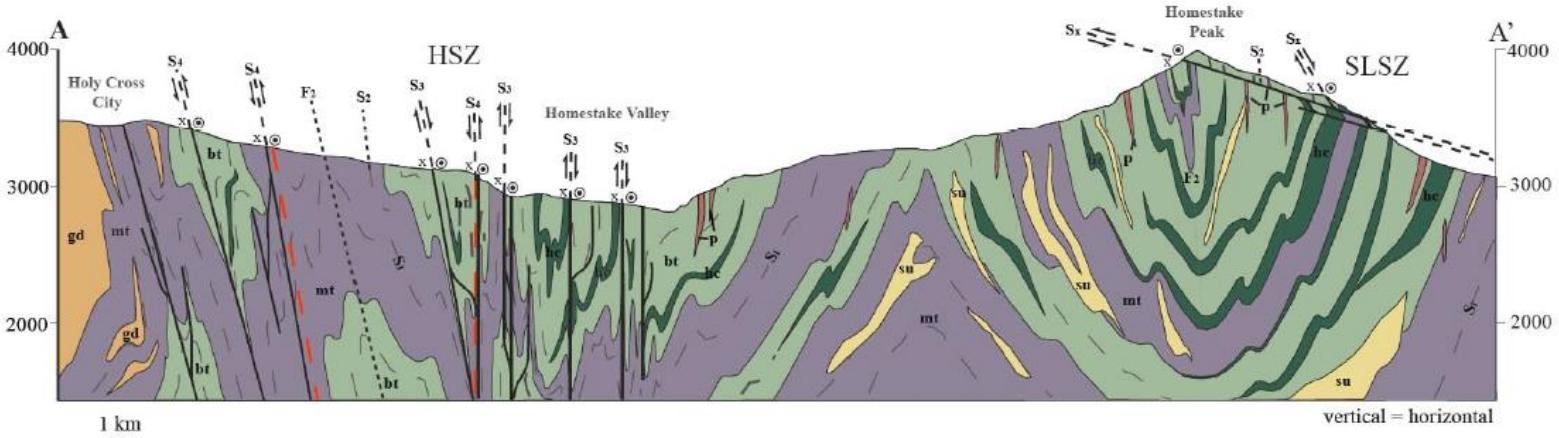

Figure 6: Geologic cross section of A'-A from Figure 5. Cross section shows multiple generations of fabrics associated with different phases of deformation. See Table 1 for descriptions of fabrics. From Lee et al. (2012)

linked, both containing mylonite that record top-down-to-the southeast, top-up-to-the northwest, and dextral movement (Lee et al., 2012).

2.3 The Homestake shear zone

The Homestake shear zone (HSZ) has been studied previously as one of the prominent regional shear zone systems within the CMB. The subvertical, northeast-striking HSZ outcrops along Homestake Creek in the Homestake Valley (Figure 5). The HSZ is characterized by several shear strands that exhibit distinct kinematics and deformation mechanisms. Consequently, the shear zone is a composite result of multiple phases of deformation at varying crustal levels throughout the Middle Proterozoic (Shaw et al., 2001). Table 1 summarizes the deformation conditions for the HSZ, using terminology from Shaw et al., (2001) (D_1-D_4) with associated fabrics for each phase of deformation.

Mesostructures of the HSZ

Deformation events recorded in rocks from the HSZ are characteristic of deformation throughout the CMB. The HSZ is comprised of a set of anastomosing splays (10 cm to 3 m-thick) of ductile shear zones that outcrop along Homestake Creek (Figure 5A, Figure 7A). Lee et al. (2012) remapped the bedrock in the vicinity of the HSZ as migmatized biotite gneiss (biotite: bt + garnet: grt + sillimanite: sil + quartz: qtz + feldspar: fsp + muscovite: ms +/- chlorite: chl), calc-silicate gneiss (hornblende: hbl +calcite: cal + qtz + fsp + ms), and alkaline mafic dikes (Tweto, 1974). The initial pulse of deformation (D_1: 1708 ± 6 Ma) is recorded by gneissic foliation (S_1) within migmatic leucosomes that resulted from high-temperature sub-horizontal flow of partially molten

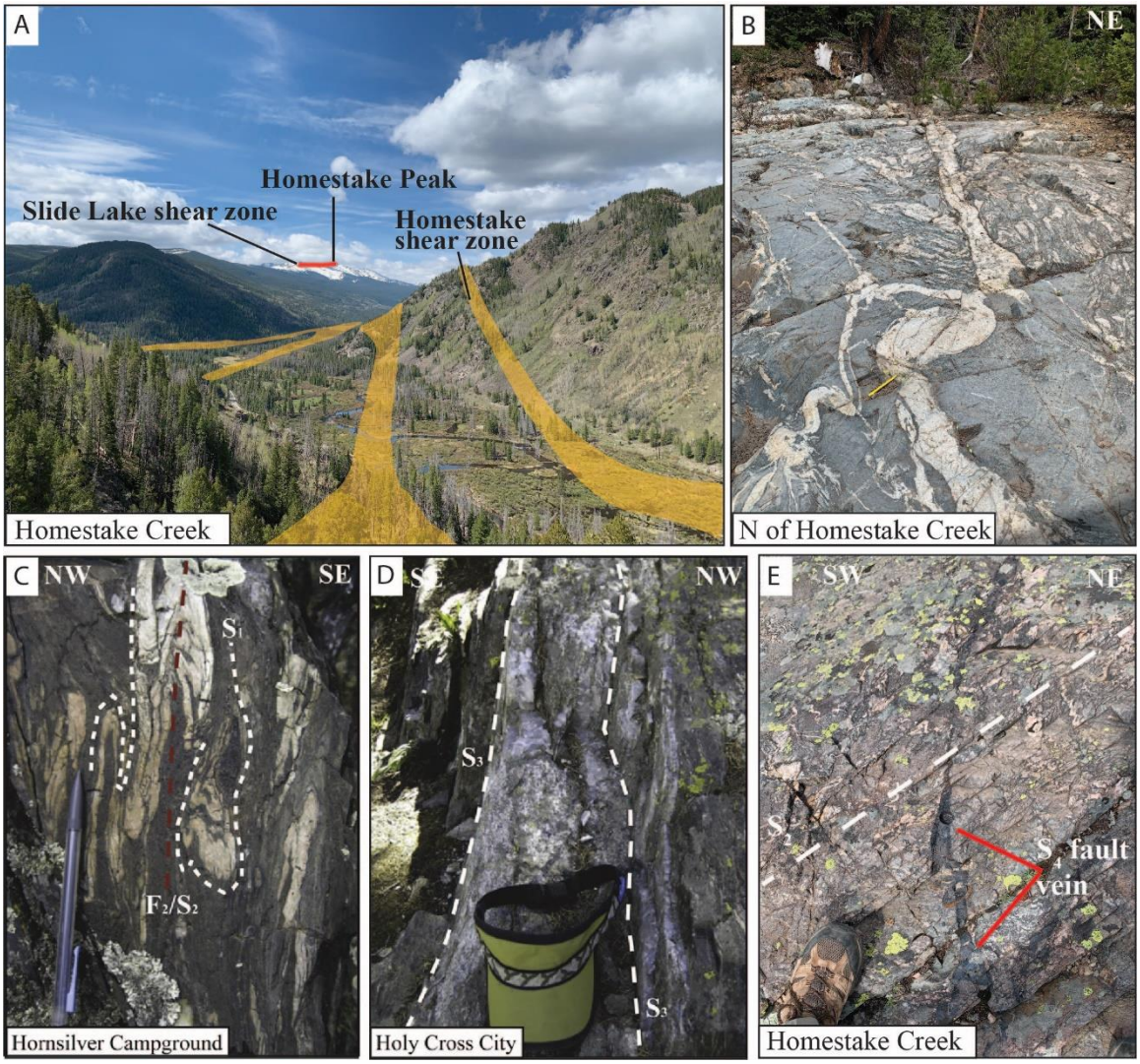

Figure 7: Characteristic mesoscale features of the HSZ. A, B, and E are from this research. C and D from Lee et al., 2012. (A.) View from Hornsilver Campground looking SW up Homestake valley along Homestake creek, subvertical HSZ shear strands are in yellow. The subhorizontal SLSZ outcrops near ridgeline on Homestake Peak. (B.) High temperature migmatite with ptygmatic folds exposed along a subhorizontal outcrop surface. (C.) S_1 foliation transposed into steep F_2/S_2 at Hornsilver Campground. (D.) Subvertical ultramylonite at Holy Cross City. (E.) Locally southeast-striking, subvertical pseudotachylyte vein overprinting subvertical S_2 fabric in biotite gneiss. Pseudotachylyte vein shows left-lateral offset. Image viewed towards the southeast.

rocks near the granite solidus (Shaw et al., 2001). S_1 foliation is present throughout much of the CMB and is present along Homestake Creek in the HSZ (Shaw et al., 2001, McCoy et al., 2005; Lee et al., 2012). The second stage of deformation (D_2) occurred in the Paleoproterozoic (1658 ± 5 Ma) and involved northwest-oriented shortening at amphibolite facies conditions. Shortening within the HSZ steepened and transposed S_1, creating a steep northeast-striking axial-surface foliation (S_2) (Figure 7C: Shaw et al., 2001). Deformation in the Mesoproterozoic is distinct from earlier phases, indicating a shift from high temperature to localized, moderate temperature (greenschist facies conditions) shear zone development that reactivated and overprinted S_2 fabrics with a prominent mylonitic foliation (S_3: 056,79°SE) with an oblique stretching lineation (L_3: 73° → 213) (Lee et al., 2012). S_3 and L_3 were observed in quartzofeldspathic rocks in the Hornsilver Campground area. Narrow mylonitic quartz-rich domains with an oblique grain-shape fabric occur in mylonite. S_3 consists of rigid porphyroclasts and shear bands that record top-down-to-the-southeast shear sense that occurred between 1.45 and 1.38 Ga (Shaw et al., 2001). The final phase of deformation (D_4) is recorded by ultramylonitic fabrics (S_4: 059, 79°SE) and pseudotachylyte that cuts S_2 and S_3 and exhibits top-up-to-the-northwest shear sense at 1375 ± 14 Ma (Shaw et al., 2001). Pseudotachylyte is distinctive to D_4 and occurs as black, aphanitic, discontinuous veins that crosscut migmatite, quartzo-feldspathic gneiss, and occur along mylonite splays (Figure 7E: Lee et al., 2012). Allen (2005) divided the pseudotachylyte zones in the HSZ into eight northeast-striking, steeply dipping zones of varying thickness that crosscut the steeply dipping S_2 foliation (059, 79°SE). The presence of pseudotachylyte is significant because

it suggests complex conditions associated with the transition from ductile to brittle deformation within an exhumed active seismic zone (Allen, 2005; Lee et al., 2012; Allen and Shaw, 2013).

Microstructures of the HSZ

HSZ mylonites (qtz + fsp + ms + bt +/- sil +/- chl) display microstructures associated with dynamic recrystallization of quartz, rigid feldspar porphyroclasts, oblique grain shape fabric in quartz (Figure 8C), mica fish, and C'- and S-C type shear bands (Figure 8A, F). In mylonite, quartz bulging (BLG) and sub-grain rotation (SGR) recrystallization textures are indicative of deformation temperatures in the range of 300 to 500°C (Lee et al., 2012: Figure 8C, E). Garnet-biotite gneiss display grain boundary area reduction (GBAR) quartz textures, corresponding to deformation temperatures above 650°C (Figure 8D). Holy Cross City splay mylonite and ultramylonite samples display a variety of shear-sense indicators such as rigid feldspar porhyroclasts, mica fish, oblique grain-shape fabric in quartz, and C'-type shear bands (Lee et al., 2012: Figure 8B). Shear-sense indicators vary, displaying top-up-to-the-northwest and top-down-to-the-southeast shear sense likely representing overprinting of earlier deformation events involving general shear or one contemporaneous deformation event involving pure shear (Lee et al., 2012).

2.4 The Slide Lake shear zone

The Slide Lake shear zone (SLSZ) is much less studied than the neighboring HSZ. Research by Lee et al., (2012) was the first to recognize the SLSZ. The SLSZ lies at the boundary between Lake and Eagle counties in central Colorado. The shear zone

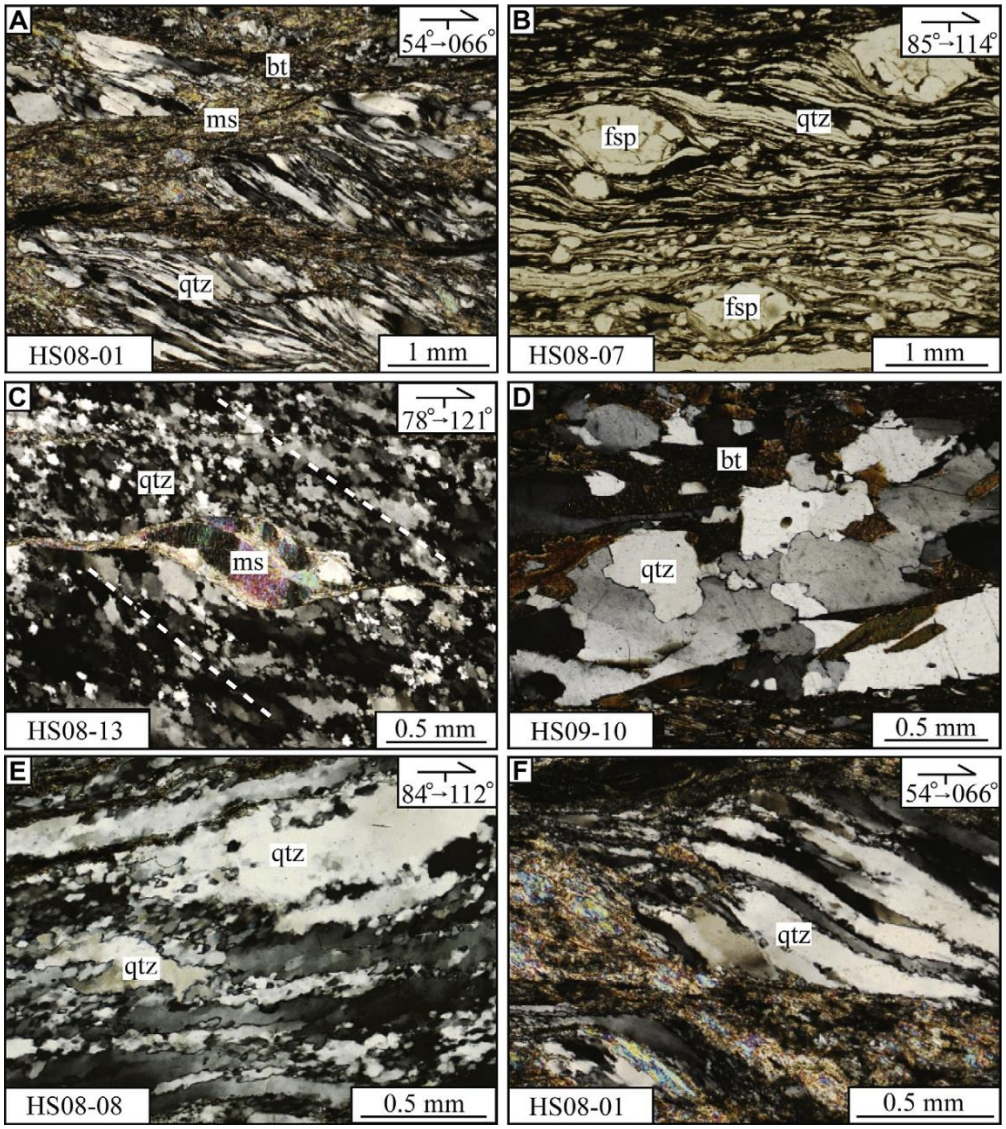

Figure 8: Microstructural observations of rocks from the HSZ from Lee et al. (2012). Orientation symbol shows trend and plunge. (A.) Ultramylonite containing S-C fabric with top-up-to-the-southeast shear. (B.) Mylonite with rigid feldspar recording top-up-to-the-northwest sense of shear; plane light. (C.) Quartz vein with oblique grain-shape fabric of quartz and mica fish that records top-up-to-the-northwest shear. (D.) Grain boundaries displaying high-temperature quartz texture (GBAR). (E.) Quartz mylonite with well-developed quartz subgrains and top-down-to-the-southeast sense of shear recorded by an oblique grain-shape fabric. (F.) Quartz mylonite with quartz displaying S-C fabric, top-up-to-the-northwest sense of shear.

outcrops approximately 1200-m-above Homestake Valley, and cuts through Homestake Peak (Figure 5 and Figure 6). The SLSZ shares a similar deformation history to the HSZ, containing Proterozoic rocks from D_1 and D_2. Similarly to the HSZ, migmatitic gneiss in the SLSZ is characterized by high temperature subhorizontal flow that steepened and transposed the S_1 fabric creating an axial surface foliation (S_2) (Lee et al., 2012). Mesoscopic shear sense indicators in mylonites and ultramylonites (e.g., rigid porphyroclasts and quartz shear bands) record top-down-to-the-southeast and top-up-to-the-northwest sense of shear (Lee et al., 2012).

Mesostructures of the SLSZ

Lee et al., (2012) mapped the Proterozoic bedrock in the vicinity of the SLSZ as amphibolite facies biotite gneiss (bt + grt + sil + qtz + fsp + ms), quartzofeldspathic gneiss (qtz + fsp + bt + ms), calc-silicate gneiss (hbl + cal + qtz + chl), and migmatite. The SLSZ was mapped as a set of mylonite and ultramylonite shear splays: (1) Bennett ridgeline, (2) Homestake ridgeline, and (3) the Slide Lake and Bennett Gulch pavement (Lee et al., (2012); Figure 5 and 9A). Lee et al., (2012) reported evidence of D_1 and D_2 (Table 1) deformation in the hanging wall and footwall of the SLSZ. Leucosomes and melanosomes of migmatitic gneiss characterize high temperature subhorizontal flow (S_1) that was subsequently steepened and transposed by D_2, creating the S_2 fabric similar to that in the HSZ. Lee et al. (2012) suggested that the prominent mylonitic fabric in the SLSZ is characterized by grain-size reduced quartz and biotite and is denoted as $S_{3(SL)}$ because it locally crosscuts S_2 in the country rock (Figure 9B, C, D). In the Bennett Ridgeline splay, quartz and feldspar aggregates define a well-developed, southeast

plunging stretching lineation ($L_{3(SL)}$: 59° → 121°) is present on the foliation surface ($S_{3(SL)}$: 048, 60°SE). Shear sense indicators from the Bennett Ridgeline splay record top-down-to-the-southeast sense of shear. The Homestake Ridgeline splay is characterized by low-angle ($S_{3(SL)}$: 003, 17°SE) greenschist facies calc-silicate ultramylonite (Figure 9D), with quartz and feldspar forming a shallowly plunging lineation ($L_{3(SL)}$: 05°→166). Shear sense indicators in this splay record two episodes of deformation, displaying both top-up-to-the-northwest and top-down-to-the-southeast sense of shear (Figure 9E; Lee et al., 2012). The Slide Lake and Bennett Gulch shear splay is comprised of high-strain mylonite and ultramylonite with similar fabrics to that of the Homestake Ridgeline splay (shallowly dipping and plunging). Shear sense in this splay is the same as in the Homestake Ridgeline splay. Exposures of ultramylonite in the SLSZ are typically much narrower (~1 cm) than mylonite zones (cm to m in width).

Microstructures of the SLSZ

SLSZ mylonites (qtz + fsp + bt + ms +/- sil) are dominated by dynamically recrystallized quartz, rigid feldspar porphyroclasts, and aligned mica grains (Lee et al., 2012: Figure 10A B). Quartz is locally segregated into narrow bands by phyllosilicate domains (Figure 10C). Deformation temperature estimates from quartz microstructures are highly variable, with samples showing BLG, SGR, grain boundary migration (GBM), and GBAR textures. Most samples display textures indicative of temperatures greater than 450°C (Figure 10D, F). Feldspar deforms differently than quartz, with porphyroclasts exhibiting microfracturing and minor core and mantle structures related to BLG recrystallization (Lee et al., 2012: Figure 10E). Shear sense is consistent

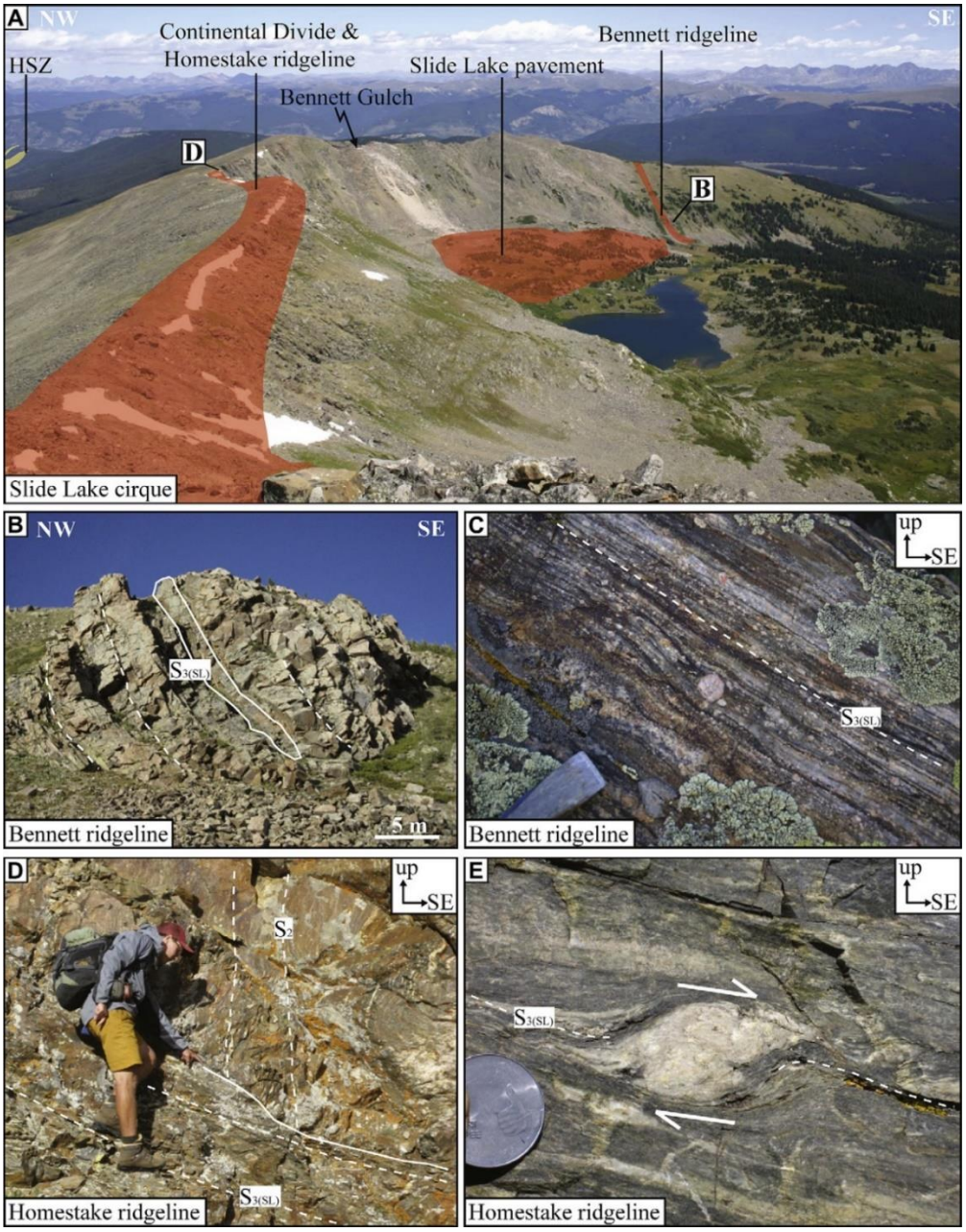

Figure 9: Field images and observations of the SLSZ, from Lee et al. (2012). (A.) Slide Lake cirque viewed from the summit of Homestake Peak. Three major splays of the SLSZ shaded red with location of field photos. (B.) Mylonite from the Bennett Ridgeline splay, outlined in white. (C.) Quartzo-feldspathic mylonite from the Bennett ridgeline with shear sense indicators in S_3 foliation with top-down-to-the-southeast shear sense. (D.) Steep S_2 fabric crosscut by the shallowly plunging foliation (S_3) of the SLSZ mylonite. (E.) Porphyroclast (top-down-to-the-southeast shear sense) within ultramylonite from the Homestake Ridgeline splay.

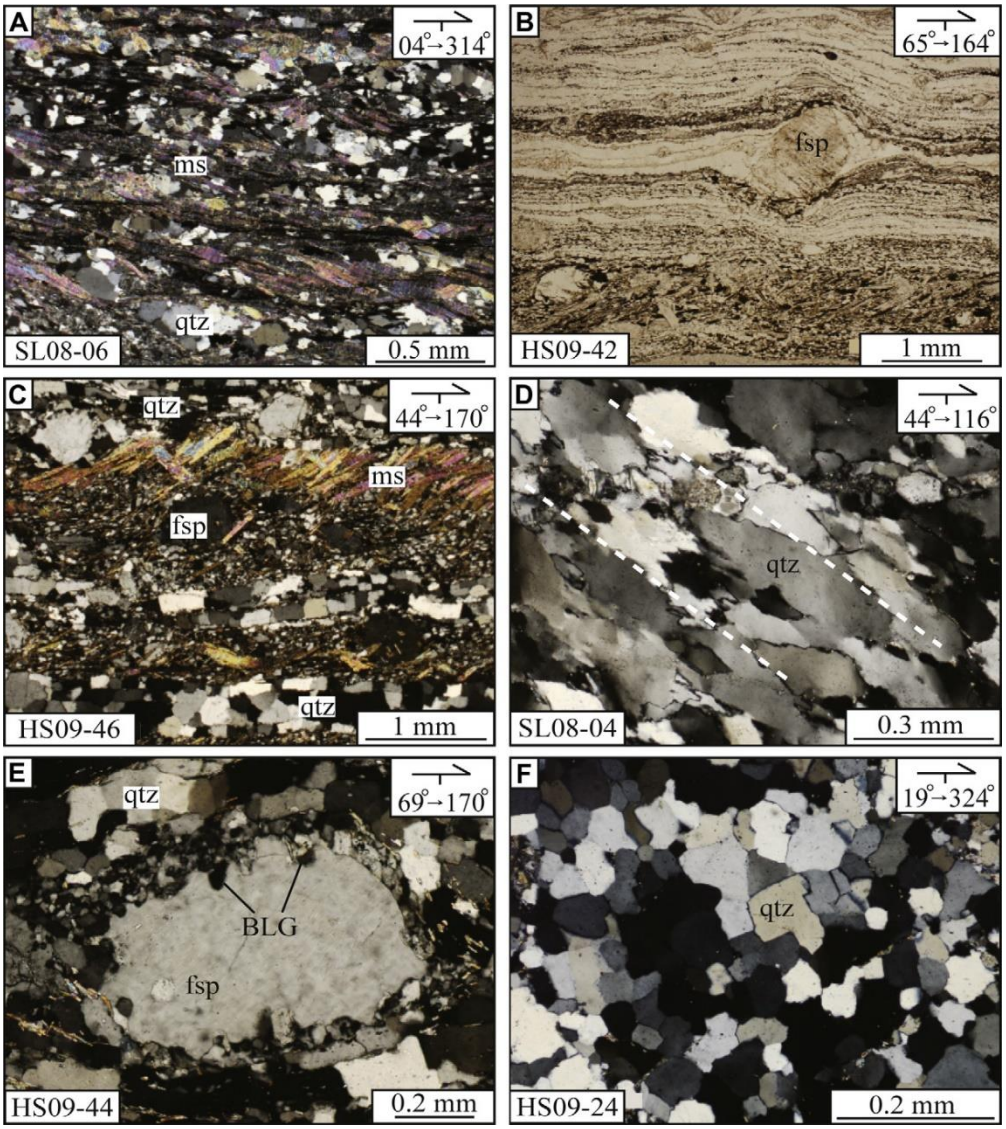

Figure 10: Microstructural observations from the SLSZ, from Lee et al. (2012). (A.) Mylonite with S-C fabric that records top-down-to-the-SE shear sense. (B.) Mylonite with rigid feldspar porphyroclasts showing top-down-to-the-SE shear sense in plane light. (C.) Mylonite with quartz domains trapped by phyllosilicates. (D.) Oblique grain-shape fabric in quartz displaying top-up-to-the-NW shear sense. (E.) Mylonite with quartz grains (GBM) and feldspar porphyroclast rims that display core and mantle structures (BLG). (F.) High-temperature quartz recrystallization texture (GBAR).

with what was seen at the mesoscale, both top-up-to-the-northwest and top-down-to-the-southeast sense of shear are recorded by asymmetric tails on rigid feldspar (Lee et al., 2012: Figure 10B), oblique grain-shape fabrics in quartz (Lee et al., 2012: Figure 10D,F), and S-C fabric (Lee et al., 2012: Figure 10A).

2.5 Kinematic framework

In the upper to middle crust, shear zones commonly develop in quartz rich rocks, and it is typically assumed that the rheology of quartz is representative of crustal rheology (Passchier and Trouw, 2005). Consequently, many of the natural and experimental studies aimed at understanding the rheology of the crust focus heavily on quartz flow laws and microstructures (e.g., Hirth et el., 2001; Toussaint et al., 2004; Lu and Jiang, 2018). Rock deformation experiments in the early 1990s provided evidence that the degree of dislocation creep in quartz relies on temperature, strain rate, and the amount of water present during deformation (Hirth and Tullis, 1992). Additionally, it was found that dynamic quartz recrystallization occurs in a predictable fashion with relation to temperature. Dynamic recrystallization of quartz occurs as grain boundary bulging (BLG, 280-400°C), sub-grain rotation recrystallization (SGR, 400-500°C), and grain boundary migration (GBM, 500-650°C). Beyond 650°C, grain boundary area reduction (GBAR) occurs typically indicating a high temperature event (Stipp et al., 2002).

Deformed quartz rich rocks often exhibit lattice orientations that are arranged in a systematic way. These rocks exhibit a *crystallographic preferred orientation* (CPO). Quartz CPOs reflect deformation conditions such as temperature, strain rate, and shear sense (e.g., Tullis & Yund, 1977; Passchier and Trouw, 2005; Pennacchioni et al., 2010).

Additionally, CPO patterns are indicative of which slip systems were active during non-coaxial progressive deformation (Figure 11A) and are temperature dependent. Lee et al. (2012) proposed a kinematic model for the HSZ and SLSZ that suggests deformation occurred at similar crustal levels within a similar tectonic regime (Figure 11).

Stretching lineations and quartz [c] axis CPO plots were used to determine movement direction and shear sense but should be used with caution in transpressional systems where along-strike variations in finite strain or strain partitioning may exist (Tikoff and Greene, 1997). Their model combines general shear in-plane strain conditions as associated with two types of movement: dextral, top-down-to-the-southeast (normal) movement (Figure 10B), and (2) dextral, top-up-to-the-northwest (reverse) movement (Figure 11C). This model supports the idea that shear zone development in the CMB resulted from transpression associated with oblique convergence along the Laurentian margin (Nyman et al., 1994; Tikoff and Teyssier, 1994; Shaw and Karlstrom, 1999; Selverstone et al., 2000; Shaw et al., 2001; McCoy et al., 2005). In this model, the HSZ vorticity vector is oriented parallel to the stretching lineation and parallel to the foliation direction (Figure 11A), corresponding to a monoclinic-transpression geometry (Figure 2). The SLSZ vorticity vector is oriented normal to the stretching lineation and parallel to the foliation direction (Figure 11A) , corresponding to a monoclinic-general shear geometry (Figure 2). Electron backscatter diffraction (EBSD) data, in the form of orientation maps and quartz orientation plots (Figure 12B), were collected by Lee (2011) for four quartz rich rocks: two quartz veins from the HSZ (HS08-12 & 13), a quartz vein from the SLSZ (SL08-04), and a quartz rich mylonite from the SLSZ (HS09-42), to

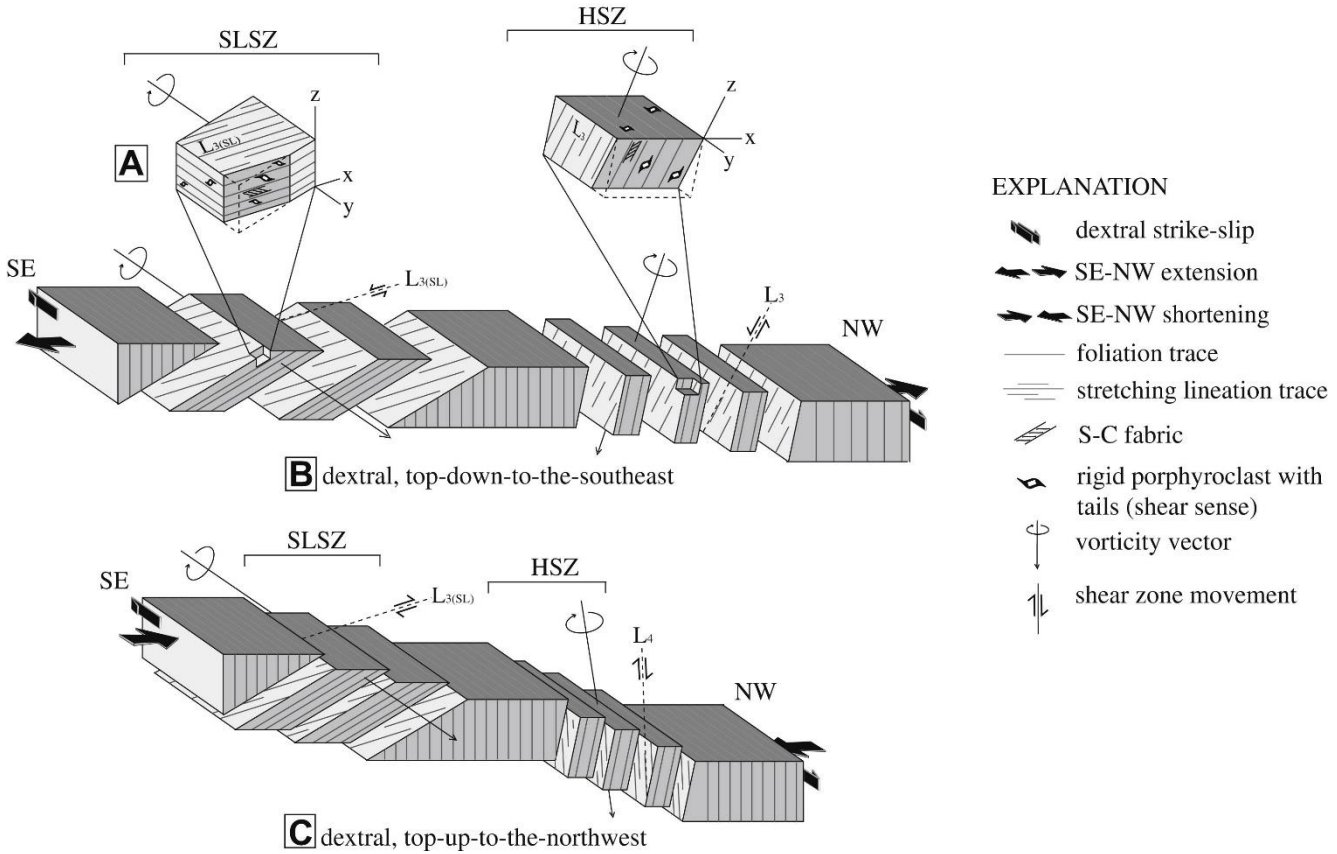

Figure 11: Schematic block diagram illustrating the kinematic model for HSZ and SLSZ, depicting several episodes of deformation. (A.) Oriented blocks from each shear zone show the XZ plane used to determine kinematics in this study. Shear sense indicators and vorticity vector denoted on the XZ plane. (B.) Kinematics of dextral, top-down-to-the-southeast deformation. (C.) Kinematics of dextral, top-up-to-the-northwest deformation. Not to scale. From Lee et al., 2012.

determine dominant slip mechanisms and infer deformation temperatures during shearing. Quartz c-axes fabrics are widely used to determine the shear plane and deformation conditions, based upon the dependence of quartz CPO and inferred slip systems on temperature and recrystallization mechanism. At lower temperatures (BLG), basal <a>, rhomb <a>, and prism <a> slip are the dominant crystal lattice slip mechanisms. Progressing into higher temperatures, SGR and then GBM dominates and basal <a> slip ceases to occur. High temperature deformation fabrics (GBAR) in quartz are present as chess-board extinction which indicates prism <c> slip. (Wilson, 1975; Mainprice et al., 1986; Law, 1990; Tullis and Yund, 1987; Stipp et al., 2002b; Nie and Shan, 2014).

CPO plots for HSZ samples (Figure 12B) reveal quartz [c] axes plotting in the center, with <a> axes plotting along the primitive circle for both samples (Lee et al., 2012). Sample HS08-12 CPO plots reveal dominant prism <a> slip, suggesting deformation temperatures greater than 500 °C. The other HSZ sample, HS08-13, CPO plots show dominant prism <a> slip with a rhomb <a> slip component that may result from slightly lower temperatures. Slip mechanisms for HS08-13 indicate higher temperatures than the temperature estimates determined from the quartz microstructures present (SGR; Figure 8C). CPO plots for the SLSZ (Figure 12C) reveal quartz [c] axes plotting in the center with <a> axes plotting around the primitive circle. Deformation temperatures inferred from CPO plots for sample SL08-04 and HS08-13 are greater than 500 °C (Lee et al., 2012).

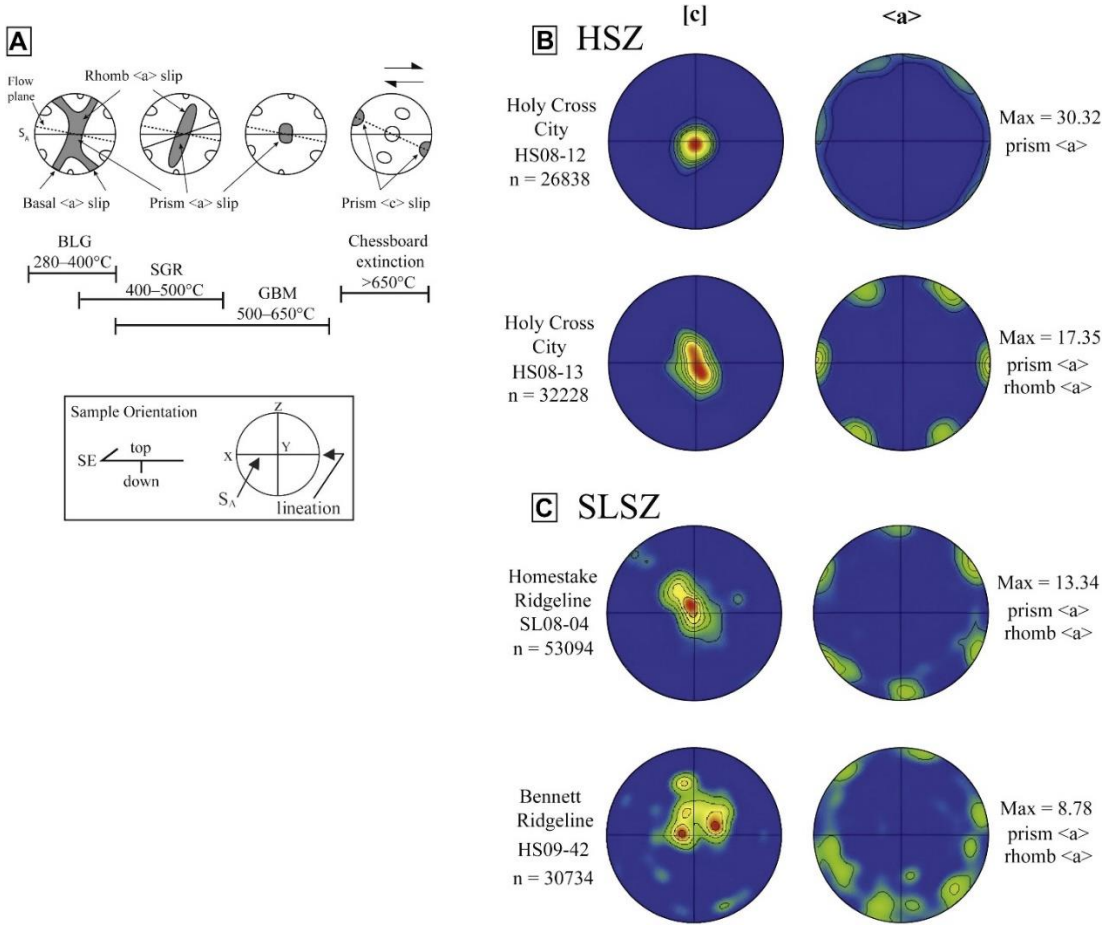

Figure 12: Quartz crystallographic preferred orientation (CPO) dependence on slip system activity and EBSD generated pole figures for the study area (A.) Stereonets showing the dependence of quartz CPOs and inferred slip systems on temperature and corresponding recrystallization mechanism during noncoaxial deformation and plain strain (after Stipp et al., 2002b; Passchier and Trouw, 2005; Langille 2010b). (B.) EBSD generated CPOs for HSZ mylonite (from Lee et al., 2012). (C.) EBSD generated CPOs for HSZ mylonite (from Lee et al., 2012).

CHAPTER 3: METHODS

This project combines field and microstructural analysis with previously and newly acquired electron backscatter diffraction data to generate estimates of the orientation of the bulk crystallographic vorticity axis for samples from the Homestake and Slide Lake shear zones in central Colorado, USA. Existing and newly obtained electron backscatter diffraction data were processed and evaluated in MATLAB to create new crystallographic preferred orientation plots along with crystallographic vorticity axis analysis. This contribution partially builds off previously collected data, primarily of which was obtained and published by Lee et al. (2012). Lee (2011) created a detailed geologic map, field context, samples, thin sections, detailed kinematics, lattice preferred-orientation plots, qualitative estimates of deformation temperatures and provided a tectonic model for the SLSZ and HSZ (Lee, 2011; Lee et al., 2012). Lee (2011) also obtained EBSD data for four mylonite and quartz vein samples, two of which are used in this study. All samples used in this study were collected during the 2008 and 2009 (Lee), and 2019 (Leierzapf) field seasons; polished thin sections were commercially prepared by *Spectrum Petrographics*. The tectonic model proposed by Lee et al. (2012) provides a framework for this research, leading to further study of the deformation conditions and geometry of the HSZ and SLSZ.

3.1 Field Visit and Mesoscale Observations

A field visit to the vicinity of the HSZ and SLSZ was completed during the summer of 2021. Five days were spent in the field area based out of Leadville, CO (in collaboration with the Concord University geology field camp, led by Joe Allen). Four of

those days were focused on mesoscale observations and mapping of the HSZ in the vicinity of the Homestake Reservoir and Horn Silver Campground (Figure 5). One day was spent exploring the Slide Lake Shear Zone in the vicinity of Slide Lake (Figure 5); late Spring snowpack made a portion of the SLSZ inaccessible. This exploration provided a geologic framework of the area and focused on representative mesoscale structural relationships between the different rock types and ages. No new field data nor samples were collected during this visit due to the availability of an existing data set.

3.2 Thin Sections and Petrography

Previously collected samples and polished thin sections, obtained during the summer of 2008-2009 by Lee et al., (2012) and the summer of 2019 by Leierzapf (2020), of highly strained rocks from the HSZ and SLSZ were investigated in this study, and are available at the University of Tennessee. Polished thin sections were produced from oriented mylonite, ultramylonite, and quartz vein samples that were collected from: (1) the SLSZ in the vicinity of Homestake Peak, (2) a transect from the southeast portion of Homestake Peak to the southeast portion of Mount of the Holy Cross, and (3) the Continental Divide Ridgeline from Homestake Peak to Camp Hale (Lee et al., 2012). The existing thin sections were cut according to the common kinematic reference frame such that they are oriented parallel to lineation and perpendicular to foliation (i.e., the X-Z plane of the strain ellipsoid). Micro- and meso-scale observations obtained by previous researchers (Leierzapf 2019 and Lee et al., 2012) provide a framework for this research, but new rock descriptions and microstructural observations were applied to all samples used for this study.

Oriented thin sections were observed and photographed using the petrographic microscope within the Structural and Tectonics laboratory in the Department of Earth and Planetary Sciences at UTK. Thin sections were analyzed for deformation fabrics and bulk mineralogy, particularly quartz-rich domains that reveal evidence of dynamic recrystallization. Samples used for EBSD analysis were selected based of the abundance of quartz and relevant microstructures and strain indicators (e.g., S-C fabrics and oblique grain-shape fabrics).

3.3 Electron Backscatter Diffraction

Electron backscatter diffraction (EBSD) is a scanning electron microscope-based crystallographic characterization technique. The EBSD setup is commonly used on polycrystalline materials and allows for the rapid obtainment of crystallographic preferred orientations (CPO), microstructural textures and fabrics, and mineralogical and compositional maps used in structural deformation studies. In geologic applications, EBSD works by targeting a polished thin section with an electron beam, and the diffracted electrons can be detected by a phosphor screen. The diffraction pattern can be digitized and is characteristic of the crystal structure and orientation (Oxford Instruments, 2015).

EBSD analysis for this study was completed by Colin A. Shaw using the HKL/Oxford Nordlys EBSD detector on the Zeiss Supra 55VP variable pressure FE-SEM housed in the Imaging and Chemical Analysis Laboratory (ICAL) at Montana State University (Bozeman, Montana). Experimental conditions were chosen for each sample to optimize signal, pattern quality, and indexing rate. Samples were tilted at 70° and

foreshortening was corrected using microscope settings. Analyses were conducted at 20 Pa with accelerating voltage of 20-30 kV, and Kikuchi pattern indexing was carried out during data collection by the HKL/Oxford Channel 5 Flamenco software (v. 5.5) and data was saved in CPR/CRC/or txt format. Indexing rates varied with a high percentage of non-indexed pixels representing surface imperfections, grain boundaries, and phases that were not included in the phase match list. Newly and previously acquired EBSD data were used to create reconstructed grain-boundary maps that are useful in evaluating crystallographic preferred orientation and necessary for crystallographic vorticity-axis analysis.

3.4 Slip System Analysis

Quartz c- and a-axis CPO plots were constructed for quartz rich samples (HS08-12, HS08-13, and SL08-04) using the existing and new EBSD data set and the MTEX toolbox for MATLAB. Pole figures of crystallographic orientation data were plotted as lower-hemisphere equal area stereonets. Separate pole figures were constructed for all quartz orientations and mean quartz grain orientations (one point per grain). Pole figure contouring represents the corresponding orientation distribution function (ODF) for each set of orientation data and is plotted as multiples of uniform density (M.U.D.) with a 10-degree halfwidth. These plots were used as an indicator of deformation temperatures and were evaluated to determine which slip systems were active during shearing. Newly constructed CPO plots were compared to the plots generated by Lee et al., (2012).

In addition to traditional quartz c- and a-axes CPO plots, the same orientation data were used to calculate low-angle intragranular misorientation axes. This method uses the

MTEX toolbox for MATLAB to extract grain boundary orientations for a specific phase from EBSD data. Low-angle intragranular misorientation axis analysis operates by isolating low angle orientations (about 2 to 15 degrees) along quartz subgrain boundaries. These data are then used to calculate a misorientation axis in the specimen reference frame, which can be used to infer slip system activity (Figure 13). This method can act as another way of inferring deformation conditions in contrast to traditional quartz CPO analysis, as it relies on intragranular orientations instead of intergranular orientations. Low-angle intragranular misorientation data were plotted on inverse pole figures as ODFs relative to the quartz crystal axes. The open-source code used for misorientation analysis was modified for this research and can be found at the *misorientations* repository on GitHub (https://github.com/zmichels/misorientations).

3.5 Crystallographic Vorticity Axis Analysis

Crystallographic vorticity axis (CVA) analysis is a relatively new method developed by Michels et al. (2015) that operates by analyzing intracrystalline distortion in sheared rocks. Grains that have been deformed at the crystal lattice scale typically preserve textures associated with dislocation accomodated strain (e.g., undulose extinction, dynamic recrystallization, annealing) that accumulates over geologic timescales in the crust. Following the definition of Kruckenberg et al., (2019) a grain is defined as an intact crystalline volume that has a distinct orientation from grains surrounding it. Crystallographic orientation maps, obtained through EBSD, are used to isolate crystallographic orientations for individual sheared grains to determine a best-fit grain-scale crystallographic vorticity axis based on orientation statistics. Michels et al.,

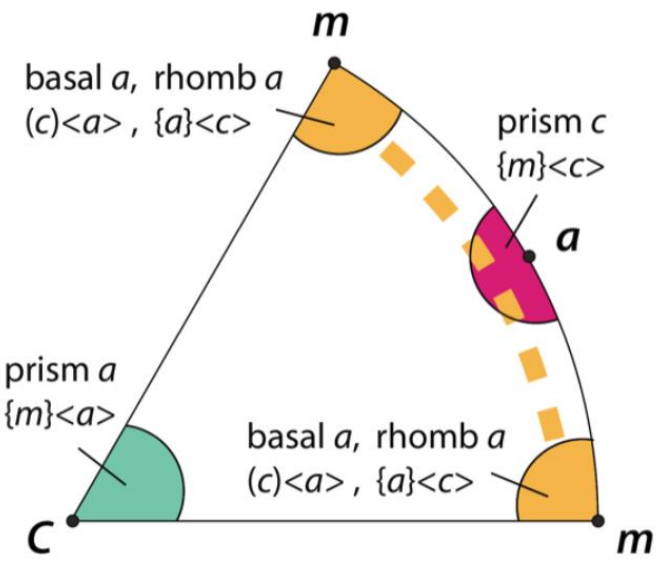

Figure 13: Plot showing the relationship between low-angle boundary orientations and slip system activity in quartz. From Flynn, MS Thesis 2021; Zachary Michels, PhD.

(2015) demonstrate that the vorticity axis of an individual grain is a pole to arcs that best describe the fit to patterns of intragranular crystallographic dispersion (Figure 14); moreover, an aggregate of individual grain-scale vorticity axes can provide an estimate of the bulk vorticity axis. CVA analysis is unique in that it does not rely on assumptions about the significance of mineral shapes and structural fabrics. Additionally, CVA analysis is not limited to monophase rocks, and can be used to better understand the kinematics of flow across various scales and lithologies (Michels et al., 2015; Kruckenberg et al., 2019).

CVA analysis was performed on two samples from the HSZ and four samples from the SLSZ using previously collected (Lee et al., 2012) and newly acquired EBSD data. EBSD data in the form .crc and .txt files were processed through MTEX for MATLAB to reconstruct maps of crystallographic texture. Orientations of grains from reconstructed maps were used for CVA analysis to determine a bulk vorticity axis that can be evaluated to further inform models of the kinematics of flow. Sample scale grain populations were analyzed, with grains defined as having three or more indexed solutions. The number of individual grains viable for CVA differs for each sample due to differences in the degree of strain, grain sizes, and EBSD resolution. Boundary grains were not excluded from the data set. CVA analysis was preformed on all indexed phases, producing an indivudal vorticity vector for each phase and a preferred "bulk" vorticity vector for the entire sample. CVA analysis was carried out using a kernel density estimation and a 10 degree halfwidth. The results of CVA analysis represent the rotational axis that describes the 3-D distortion of an indivudal grain at the crystal lattice

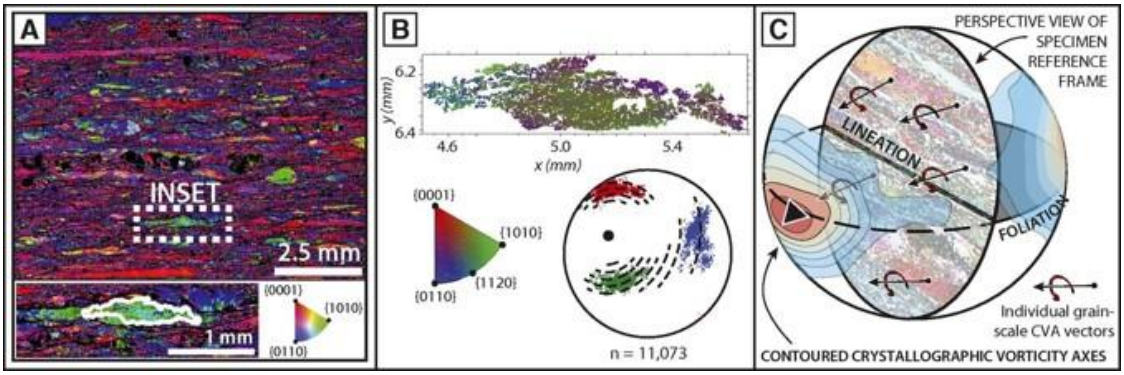

Figure 14: Crystallographic analysis method. (A.) Orientation map of sample SL35–02 from the Moine thrust zone (northeast Scotland). Inset shows detail region containing the example grain (white outline). (B.) Isolated grain data colored by orientation relative to the x axis of the map; lower hemisphere projection of intragranular orientations showing the principal axes of the crystallographic unit cells (red, green, blue dots); and derived intragranular vorticity axis (black dot). Dashed arcs of small circles are projected from the calculated axis to show that rotation about the dispersion axis matches the spread of crystallographic orientations. (C.) Perspective spherical schematic illustrating the kinematic framework in the sample. CVA—crystallographic vorticity axis. From Michels et al. (2015).

scale. Vorticity axes are thought to be reset rapidly compared to the geologic timescales over which deformation occurs. Therefore, it is assumed that these axes represent a record of instantaneous rotation, effectively recording the most recent event affecting the grain (Michels et al., 2015: Kruckenberg et al., 2019). A key assumption of CVA analysis is that individual grains provide a record of instantaneous crystal-plastic deformation and reflect specimen-scale deformation that can be used to interpret mesoscopic kinematics such as shear-zone geometry (Michels et al., 2015). Since its inception by Michels et al. (2015), CVA analysis has been used as a modern approach to answer questions regarding kinematics at a variety of tectonic settings by several researchers (e.g., Girogis et al., 2016; Schmidt et al., 2016; Kruckenberg et al., 2019; and Flynn, MS Thesis 2021). This application of CVA was made possible through the use of open-source code available at the *CVA* reposity on GitHub.

3.6 FABRICA Analysis

FABRICA analysis, developed by Zachary Michels, is a MATLAB-based method for rotating crystallographic data, collected in a specimen reference, to an overall geographic reference frame (Kruckenberg et al., 2019). Sample scale CVA analyses were rotated from the specimen reference frame to a common geographic reference frame using 3-D fabric elements (i.e., strike and dip; trend and plunge) measured by Lee et al. (2012). Only samples with strike, dip, trend, and plunge measurements can be rotated. Rotating to a geographic reference frame is important because it permits the comparison of crystallographic data to regional scale analyses. Kruckenberg et al. (2019) used rotated fabric analyses and vorticity estimates to constrain the orientation of the convergence

vector between the Nashoba and Avalon terranes in southeast New England. This research does not attempt to estimate a convergence vector for the Yavapai terrane but rotating to a geographic reference frame provides insight into regional deformation. The code used for FABRICA analysis is available for public use at the *Fabrica* repository on GitHub (https://github.com/zmichels/Fabrica) .

CHAPTER 4: RESULTS

Six samples previously collected by Lee et al. (2012) were chosen for CVA analysis (Table 2: HS08-12, HS08-13, SL08-04, HS09-21, HS09-23, and HS09-29). Microstructural data collected by Lee et al. (2012) was used as a guide for sample selection and was reevaluated during this research (Table 2). The samples were selected depending on abundance of quartz and deformation textures, as well as viability for further EBSD analysis depending on the presence of a cover slip. The samples selected for EBSD analysis include two quartz veins from the Holy Cross City (HSZ) ultramylonite splay (HS08-12 and HS08-13), a quartz vein from Homestake Peak (SLSZ: SL08-04), and three quartz mylonite samples from the Slide Lake Cirque splay (SLSZ: HS09-21, HS09-23, and HS09-29) (locations in Figure 5). Deformation conditions were reevaluated using quartz deformation textures, mineral assemblages, and shear sense. All oriented samples were viewed in the common kinematic reference frame: parallel to lineation, perpendicular to foliation (XZ). Here I present sample descriptions, quartz c-axis preferred orientation plots, low-angle intragranular misorientation axis analysis plots, and CVA analysis plots.

4.1 Petrography and Sample Descriptions

HS08-12

Sample HS08-12 is a mylonitic quartz vein consisting of SGR quartz textures (400–500 °C) and mica (ms) fish (Figure 15). A prominent oblique grain-shape fabric in quartz is present throughout the sample. Mica fish and oblique grain-shape fabric display top-up-to-the-northwest sense of shear. Temperature estimates and shear sense are

consistent with the most recent episode of deformation (D_4) at ~1.38 Ga. This sample was considered viable for CVA analysis due to the abundance of quartz. Quartz slip-system analysis was preformed using the existing data set.

HS08-13

Sample HS08-13 is a quartz vein collected in close proximity to HS08-12. Much like HS08-12, this sample is comprised of dynamically recrystallized quartz and sheared muscovite (Figure 16). Quartz grain boundaries are serrated and indicative of SGR (400–500 °C). An oblique grain shape fabric in quartz persists throughout the sample, suggesting deformation involved top-to-the-northwest sense of shear. This sample had previously acquired EBSD data that was used to reevaluate quartz [c] and <a> axis plots and to conduct CVA analysis.

SL08-04

Sample SL08-04 is a high-strain quartz vein from the SLSZ displaying top-to-the-northwest sense of shear (Figure 17). Deformation temperatures are in the range of 450–550 °C, representing the transition from SGR to GBM recrystallization. The matrix is comprised of quartz undergoing SGR recrystallization. An oblique grain-shape fabric in quartz is present locally and exhibits GBM recrystallization textures (Figure 16B and C). Potassium feldspar is present and is altered to white mica (sericite) (Figure 16A). Shear sense was determined from discontinuous feldspar domains and recrystallized quartz domains.

Table 2: Summary of Microstructural Analysis

HSZ and SLSZ relevant sample locations and structural data from Lee et al., (2012). Abbreviations: HCC, Holy Cross City; HP, Homestake Peak; SLC, Slide Lake Cirque; BR, Bennett Ridgeline, DD, Down Dip; qtz.v., quartz vein; my, mylonite; t-NW, top-up-to-the-northwest; t-SE, top-down-to-the-southeast. Temperatures from quartz microstructures and/or mineral assemblages

Sample	*Location*	*Latitude*	*Longitude*	*Strike*	*Dip*	*P→T*	*Rock Type**	*Shear Sense**	*Temp. (C°)**
HS08-12*	HCC	39.4189	-106.4733	023	84SE	DD→113	qtz.v	t-NW	450-500
HS08-13*	HCC	39.4189	-106.4733	031	78SE	DD→121	qtz.v	t-NW	450-500
SL08-04	HP	39.3671	-106.4175	002	65SE	N/A	qtz.v	t-NW	450-550
HS09-21	SLC	39.3758	-106.3973	120	12 N	7→320	my	t-SE	350-500
HS09-23	SLC	39.3758	-106.3973	123	7NE	7→324	my	t-SE	550 - 650
HS09-29	SLC	39.3718	-106.4029	065	43 N	41→312	my	t-SE	>600

* Rock types, shear sense, and deformation temperatures were reevaluated during this research. Data for HS08-12 and HS08-13 were collected by Lee et al. (2012).

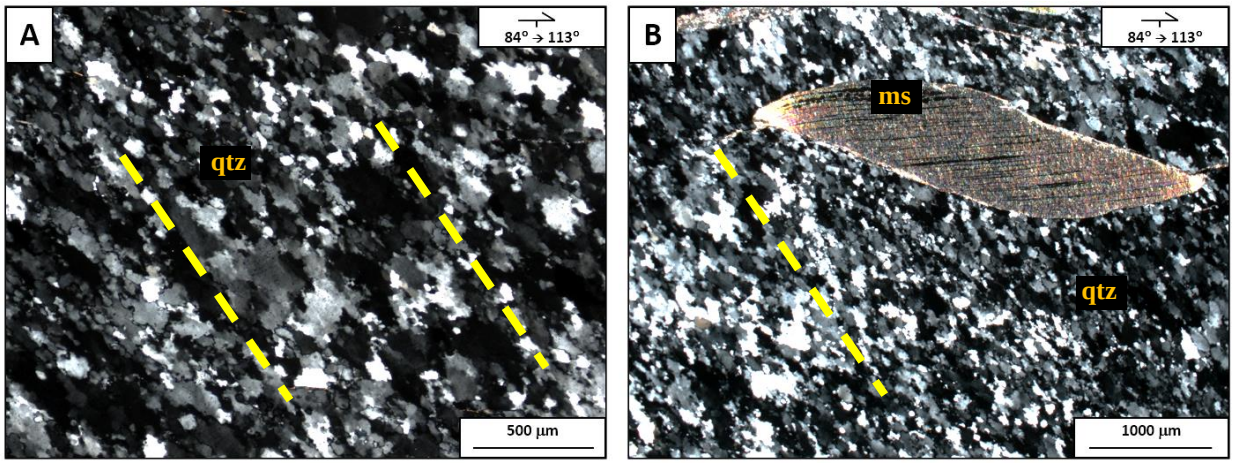

Figure 15: Sample HS08-12 photomicrographs, XPL. (A.) Quartz oblique grain shape fabric at a steep angle to foliation; t-NW sense of shear. (B.) Mica fish surrounded by recrystallized (SGR) quartz grains. Sense of shear is t-NW.

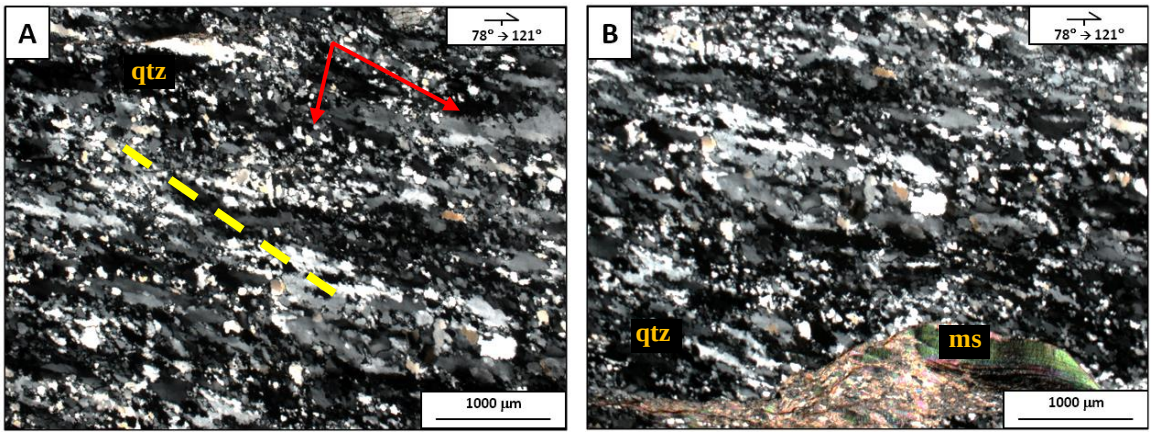

Figure 16: Sample HS08-13 photomicrographs displaying t-NW sense of shear, XPL. (A.) Fine grained quartz (red arrows; SGR) with an oblique grain shape fabric at a moderate angle to the dominant fabric. (B.) Mica fish surrounded by quartz subgrains.

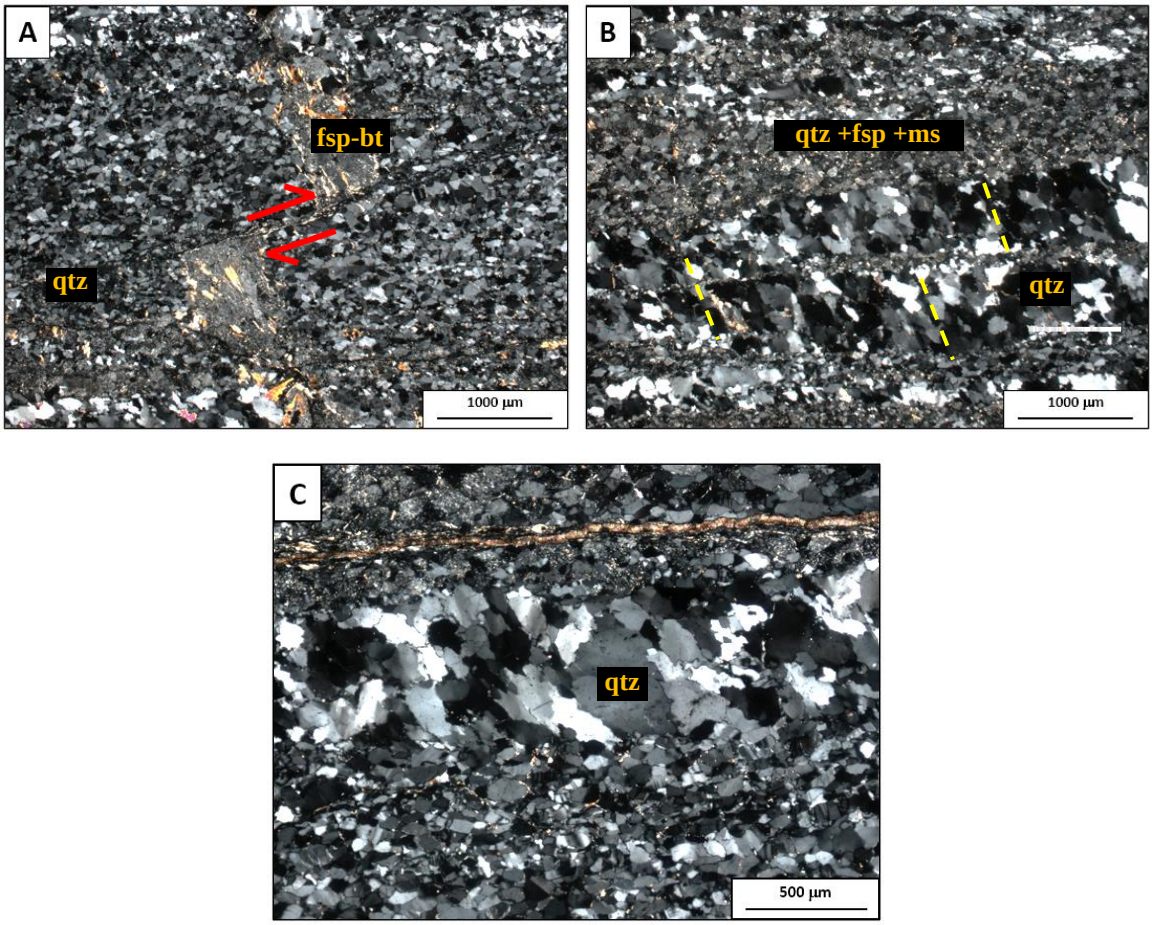

Figure 17: Sample SL08-04 photomicrographs. (A.) Discontinuous feldspar grain exhibiting right lateral offset; t-SE sense of shear. (B.) Quartz subgrains with an oblique grain shape fabric surrounded by feldspar, mica, and quartz. (C.) SGR and GBM textures in quartz.

HS09-21

Sample HS09-21 is a mylonite (qtz+fsp+ms+bt) consisting of BLG and SGR quartz textures (Figure 18: 350–500 °C). Opaque minerals are likely magnetite. Muscovite-rich layers are subparallel to the mylonitic fabric, appearing to pin dynamically recrystallized quartz. A weak S-C fabric is evident by the alignment of phyllosilicates (bt and ms), suggesting top-down-to-the-southeast shear sense (Figure 17). CVA analysis was conducted on all indexed phases.

HS09-23

Sample HS09-23 is a mylonite (qtz+fsp+musc+bt+sil) dominated by high-temperature sillimanite and dynamically recrystallized quartz fabrics (Figure 19: GBM and GBAR – 650+°C). Relict sillimanite porphyroclasts are surrounded and partially filled by swaths of mica. Muscovite is likely a retrograde product based on its association with sillimanite, and can be explained by the reaction (Equation 1):

$$KAlSi_3O_8 + Al_2SiO_5 + H_2O = KAl_2AlSi_3O_{10}(OH)_2 + SiO_2 \quad (1)$$

The presence of sillimanite indicates an earlier high temperature (≥550 °C) deformation event. Sillimanite porphyroclasts and mica fish exhibit top-down-to-the-southeast shear sense, consistent with what was reported by Lee et al. (2012).

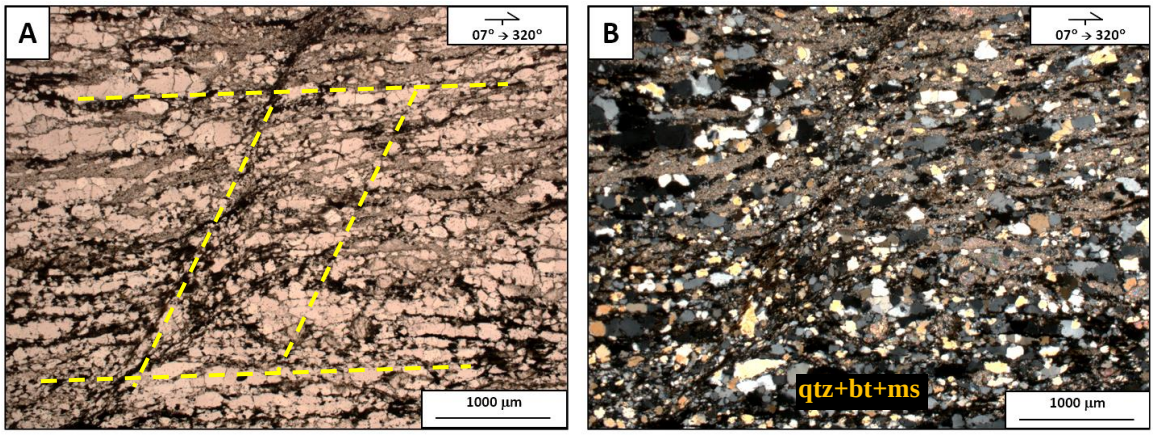

Figure 18: Photomicrographs of sample HS09-21. (A.) Plane-polarized light image showing phyllosilicate layering and a weak S-C fabric (dashed yellow line). (B.) Cross-polarized light image of the same area showing a recrystallized quartz pinned by mica.

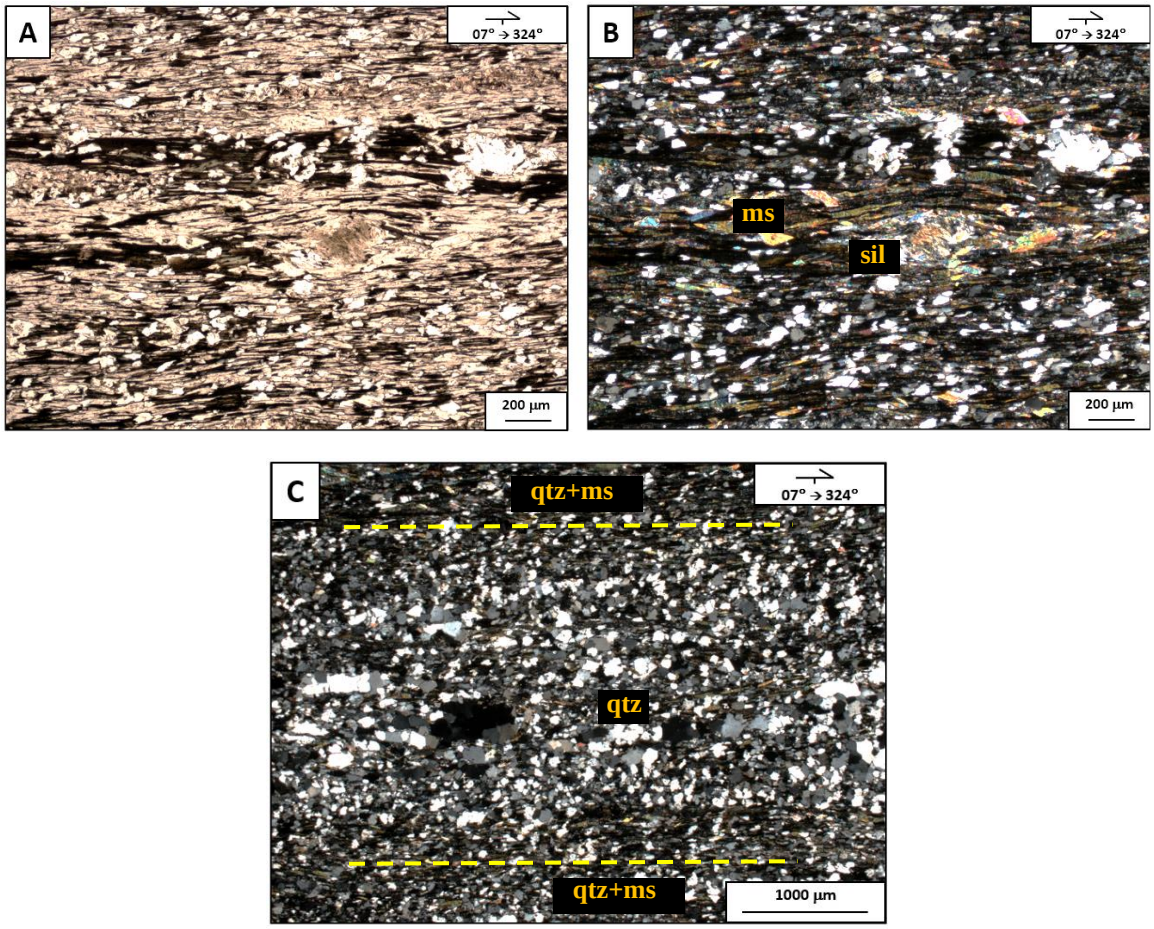

Figure 19: Photomicrographs of sample HS09-23. (A&B). Sillimanite porphyroclast in contact with muscovite within a recrystallized quartz matrix. A- PPl, B-XPL. (C.) Recrystallized quartz domain bounded by quartz and mica layering. Quartz exhibits GBM recrystallization textures, XPL.

HS09-29

Sample HS09-29 is a mylonite (qtz+fsp+sil+ms+bt+mag) consisting of high-temperature deformation textures and high-temperature mineral assemblages (Figure 20). Sillimanite is closely associated with muscovite that likely formed via the retrograde reaction (Equation 1). Asymmetric tails of muscovite on sillimanite prophyroclasts indicate top-down-to-the-southeast shear sense. High-temperature quartz domains (GBAR) are surrounded by SGR quartz, indicating temperatures ≥600°C (Figure 20C).

4.2 Slip-System Analysis and Deformation Temperature Estimates

Quartz C- and A-axis Crystallographic Preferred Orientation Plots

Quartz c- and a-axes plots were regenerated using the EBSD data set obtained by Lee et al. (2012) as well as the new EBSD data set acquired during this research (Figure 21). These plots were used to determine if quartz exhibits a crystallographic preferred orientation in each sample, which can be used to evaluate slip system activity and deformation temperature. In the HSZ, Lee et al. (2012) documented that quartz CPOs reveal dominant prism <a> slip and a minor rhomb <a> slip component. The regenerated CPOs for HSZ samples, from the Holy Cross City mylonite, are consistent with what Lee et al. (2012) determined, with c-axes plotting around a central girdle or point maximum, and a-axes plotting around the primitive. The presence of a point maxima presents slip along prism <a> while a central girdle is evidence of prism <a> and rhomb <a> slip (Figure 12A). Sample HS08-12 exhibits a quartz CPO pattern consistent with

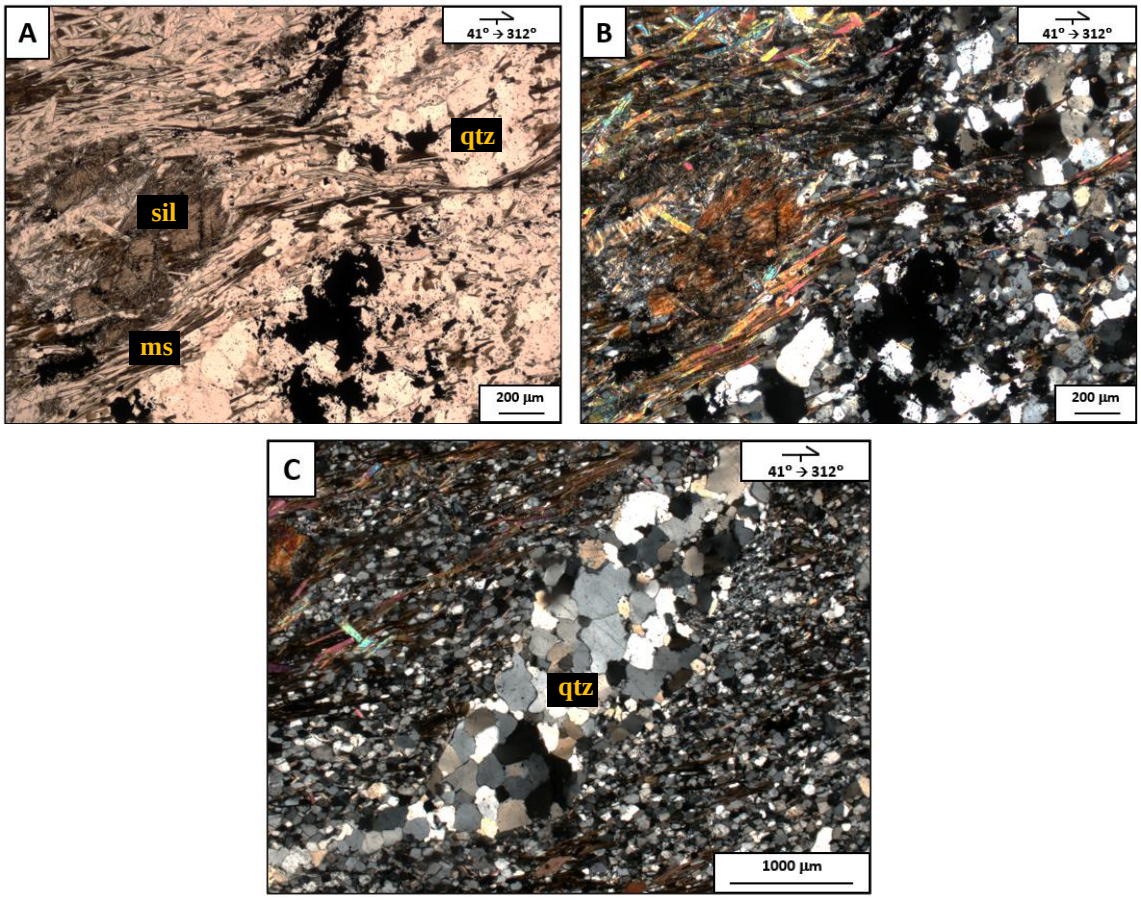

Figure 20: Sample HS09-29 photomicrographs. (A&B.) PPl and XPL images of sillimanite surrounded by retrograde mica within a matrix of recrystallized quartz. (C.) XPL image of GBAR quartz within a matrix of SGR quartz.

temperatures between 500–650°C (Figure 21). Sample HS08-13 reveals dominant prism <a> slip with a minor component of rhomb <a> slip. In agreement with what was reported by Lee et al. (2012), the deformation temperatures derived from quartz CPOs are higher (Figure 21: ≥500°C) than temperature estimates from the prominent quartz subgrain texture (Figure 15: 400–500°C). CPOs for HSZ samples plot within the plane of foliation. Sample SL08-04, from the SLSZ, exhibits a strong quartz CPO pattern with a central point maximum plotting around the center and a second mode of crystallographic orientations plotting to the southwest of the central maximum. SL08-04 displays CPOs consistent with dominant prism <a> and a minor rhomb <a> slip component, in agreement with what was reported by Lee et al. (2012) (Figure 12). New CPO plots for samples from the Slide Lake Cirque splay of the SLSZ exhibit distinct patterns from the HSZ samples. HS09-21 displays a weak CPO (Max = 2.0) plotting away from the center but still in the plane of foliation, indicating possible prism <a> slip (Figure 21). Sample HS09-23 exhibits a strong CPO plotting along the great circle, suggesting that slip system activity was dominated by prism <c> slip. In comparison to sample HS09-21, sample HS09-29 displays a slightly stronger, although weak, CPO (Max = 2.3) above the center in the plane of foliation, indicating possible prism <a> slip. (Figure 21).

Low angle intragranular misorientation axis analysis

Traditionally, quartz c-axis CPO plots are used to infer slip-system activity and temperature estimates during deformation A new method developed by Zachary Michels (https://github.com/zmichels/misorientations), uses MTEX to extract low-angle boundaries between grains to evaluate slip systems and temperatures.

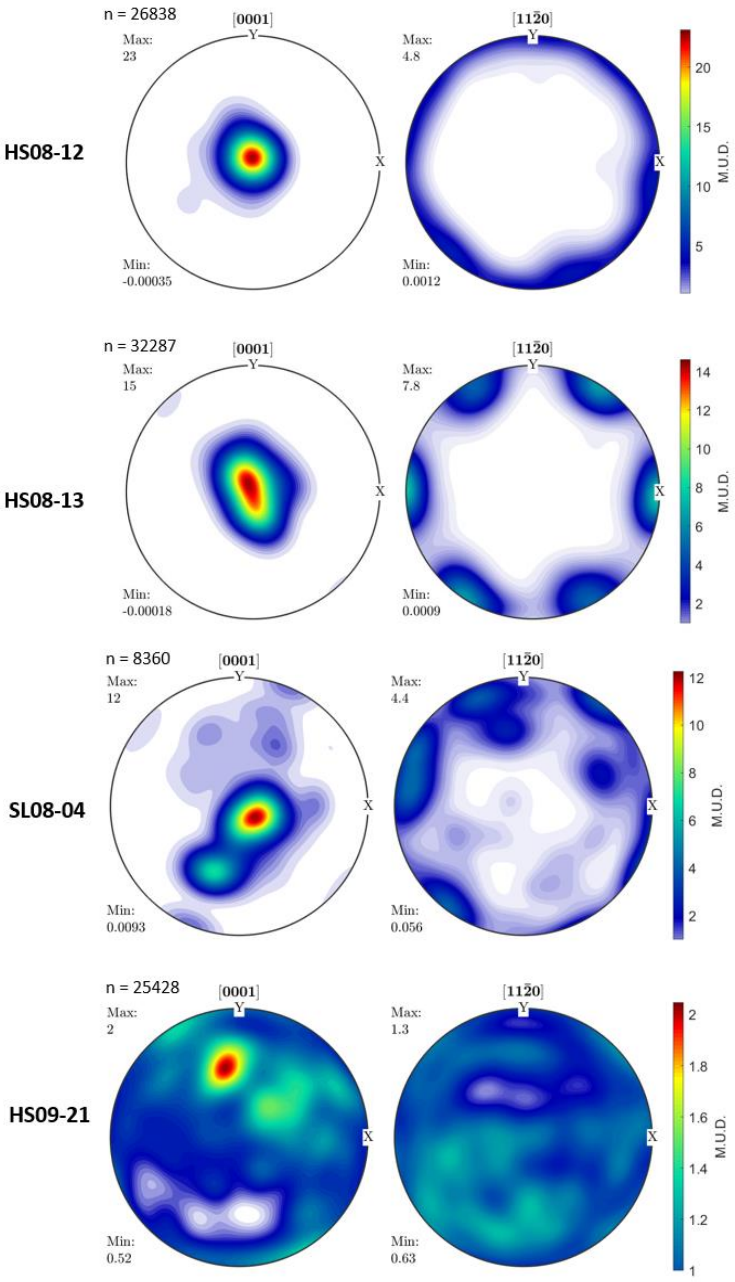

Figure 21: Lower hemisphere equal area pole figures of Quartz c- and a-axis orientations used to determine quartz CPO patterns. Plots are color contoured (multiples of uniform density, M.U.D.), with a 10-degree halfwidth, representing the corresponding orientation distribution function for each set of orientations. Plots are viewed in the specimen reference frame (parallel to lineation, perpendicular to foliation). N represents number of orientations. Y and X directions are an artifact of importing the EBSD data into MTEX.

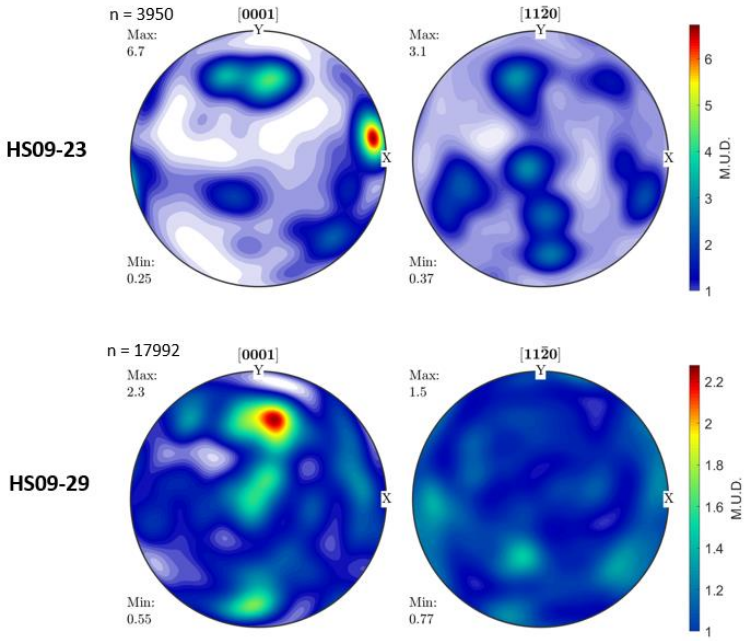

Figure 21 (Continued)

This method was applied to six samples with electron backscatter diffraction data. These plots (Figure 22) can be interpreted and compared to existing CPO derived slip system and deformation temperature estimates. Misorientation axes for the HSZ, samples HS08-12 and 13, display dominant prism <a> slip with HS08-13 displaying a weak rhomb <a> slip pattern. This agrees with the slip systems determined using CPO patterns. Samples from the SLSZ display a variety of slip-system patterns. Sample SL08-04 displays a strong maximum around the [0001] axis corresponding to prism <a> slip, but does not appear to exhibit rhomb <a> slip as seen in the corresponding CPO plot. SLSZ sample HS09-21 displays a strong maximum around the [-1100] axis, indicating possible basal <a> and rhomb <a> slip. Sample HS09-23 displays a weak (N = 11) concentration of misorientations around the [-1100] axis indicating basal <a> and rhomb <a> slip but shows no c-axis pattern as seen in the CPO plot (Figure 21). Sample HS09-29 did not yield enough neighbor-grain orientations to allow for misorientation analysis.

4.3 Crystallographic vorticity axis analysis

Crystallographic vorticity axis analysis was performed on 6 samples using the method developed by Michels et al. (2015), and existing and newly acquired EBSD data. CVA analysis was conducted using the MTEX toolbox for MATLAB. Bulk CVA plots are given in the specimen reference frame in Figure 23, showing that the bulk vorticity axis (black dot) lies approximately in the center for samples HS08-12 and HS08-13. In these samples, the vorticity-normal surface is oriented approximately horizontal and parallel to the XZ plane. The orientation of the vorticity axes shows that the Holy Cross

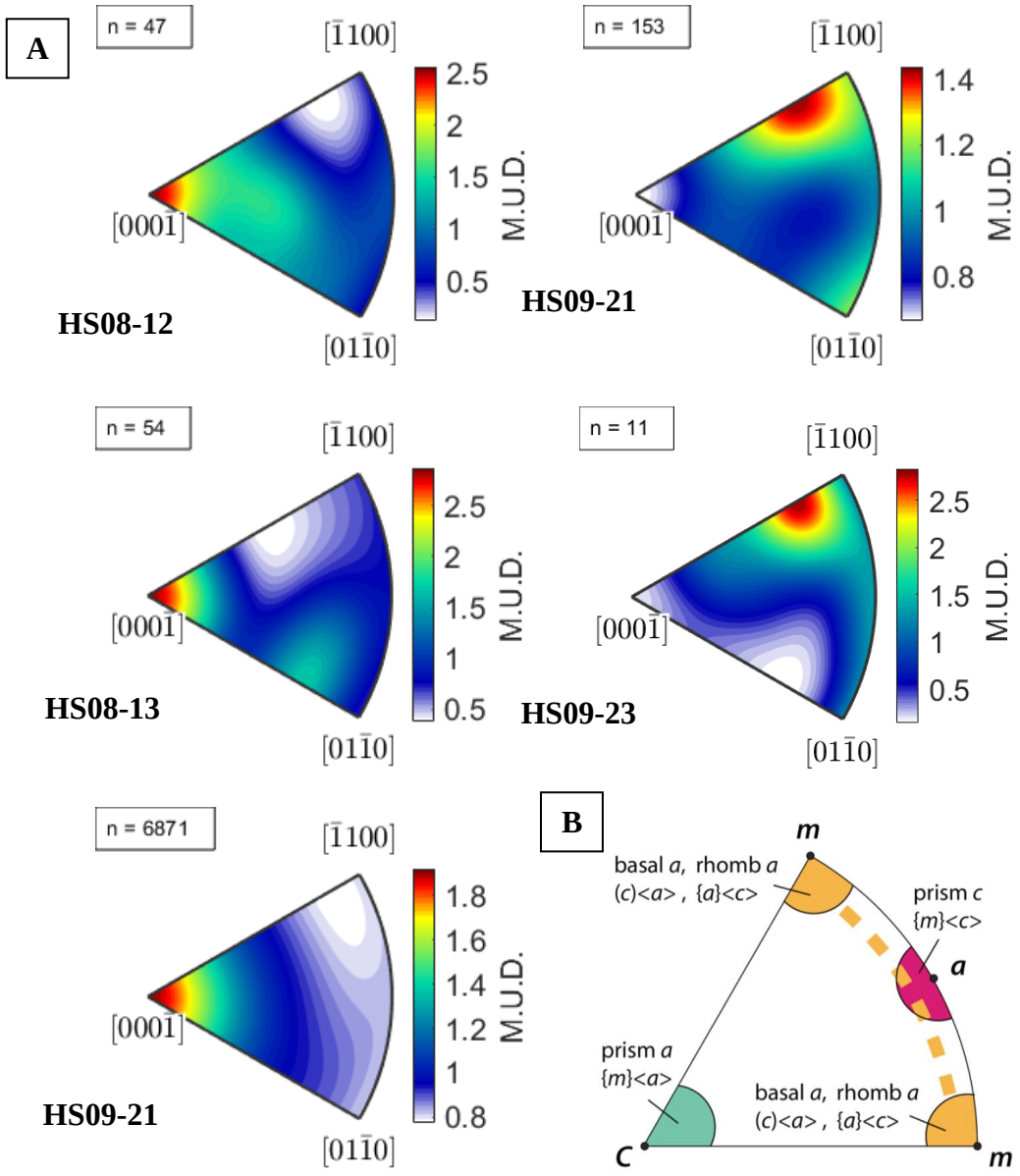

Figure 22: Wedge plots showing the results of quartz low-angle, intragranular boundary misorientation analysis. (A.) Wedge plots color contoured using an orientation distribution function within the crystal reference frame for each sample. N is number of orientations analyzed. (B.) Explanation of wedge plots, showing corresponding slip system activity.

City splay of the HSZ exhibits a monoclinic shear zone geometry; the vorticity vector plots normal to the XZ plane (parallel to the steeply plunging lineation). CVA plots for the Homestake Ridgeline splay of the SLSZ (sample SL08-04) indicate that the vorticity-normal surface is oblique to the XZ plane (the vorticity vector is oblique to lineation). Therefore, the bulk vorticity axis plots out of the XZ plane. The orientation of the bulk vorticity axis calculated for the Slide Lake Cirque splay of the SLSZ (Figure 23: HS09-21,23,29) is evident by girdled or oblique point maxima, but none of these samples reveal point maxima oriented normal to the XZ plane. On a stereographic projection, the vorticity-normal surface (black great circle; Figure 23) for samples HS09-21 and HS09-29 strikes west whereas the vorticity-normal surface for sample HS09-23 strikes northeast. The dominant phase within the HSZ samples is quartz, therefore the bulk CVA orientation of the HSZ is controlled by quartz. The major phases within the SLSZ are variable, with lithologies being nearly all quartz (SL08-04), or polyphase consisting of feldspar, quartz, biotite, and magnetite (excluded in CVA analysis due to low number of grains). CVA plots for each of the major phases in the SLSZ are similar to the bulk CVA plot for each sample (Figure 24). Among the other phases, CVA analysis plots for microcline and quartz most closely match the bulk CVA axis plots. In contrast, biotite and orthoclase CVA plots show the most deviation from the bulk CVA plots, often exhibiting multiple modes of crystallographic dispersion axes (Figure 24). This could be due to the lower abundance of biotite and orthoclase.

4.4 FABRICA Analysis

Rotated CVA Plots

Samples with documented foliation and stretching lineation data were rotated from the specimen reference frame (XZ plane) to an overall geographic reference frame, defined by the strike and dip and trend and plunge of fabric elements, using the FABRICA analysis add on for the MTEX toolbox in MATLAB. Figure 25 offers another way of looking at the CVA analysis results. The plots shown have been rotated to a geographic reference frame. The orientation of the vorticity-normal surface for HSZ is generally the same. SLSZ samples HS09-21 and -29 are generally the same, with HS09-23 displaying the inverse orientation, like seen in Figure 23. Previous research (Kruckenberg et al., 2019) has shown that rotated CVA plots can be combined with ISA and flow apophysis orientations along with oblique grain-shape analysis to determine a paleoconvergence vector. Paleoconvergence reconstruction was not conducted due to the absence of an oblique grain-shape fabric in all samples. A strong oblique grain-shape fabric can be used to estimate flow parameters such as the orientation of ISAs and flow apophyses, as well as provide estimates on the ratio of pure- to simple-shear.

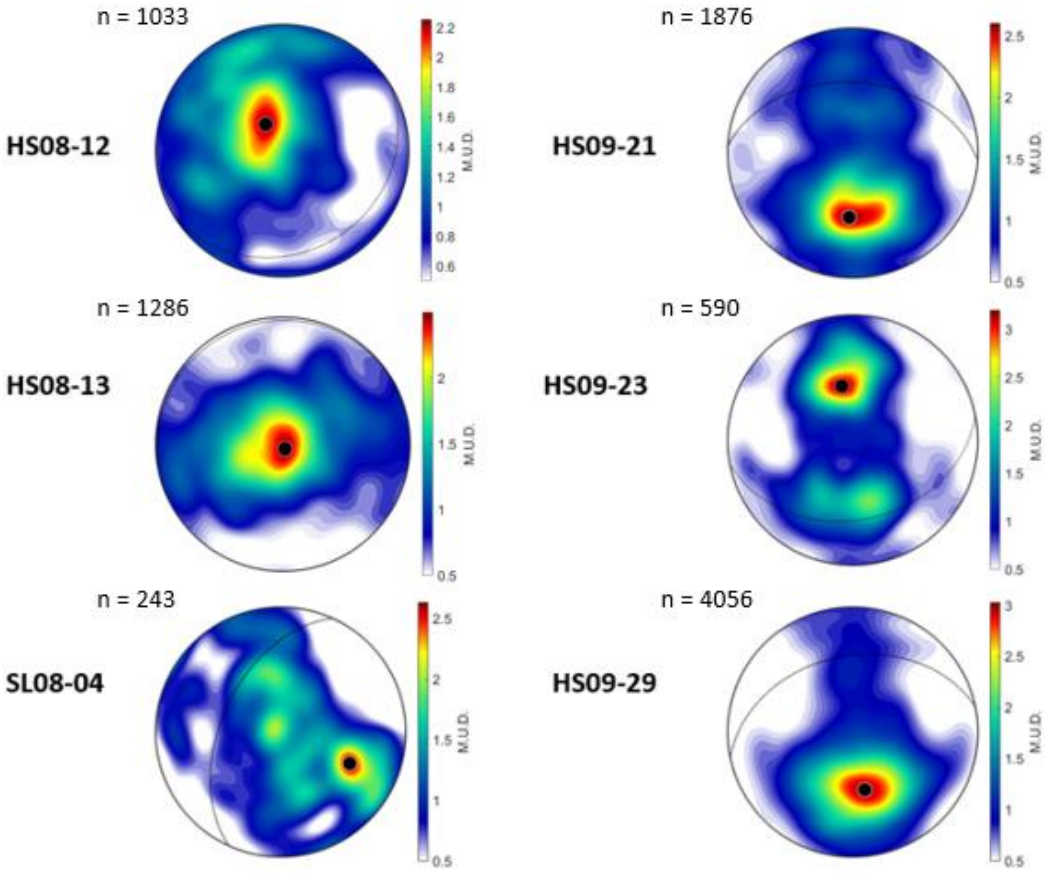

Figure 23: Lower hemisphere, equal area stereonets showing the orientation of the bulk vorticity axis (black dot) and vorticity normal surface (black great circle) determined through crystallographic vorticity axis analysis. Plots are color contoured (multiples of uniform density, M.U.D.), with a 10-degree halfwidth, representing the corresponding orientation distribution function for each set of orientations. N represents number of grain-scale axes analyzed.

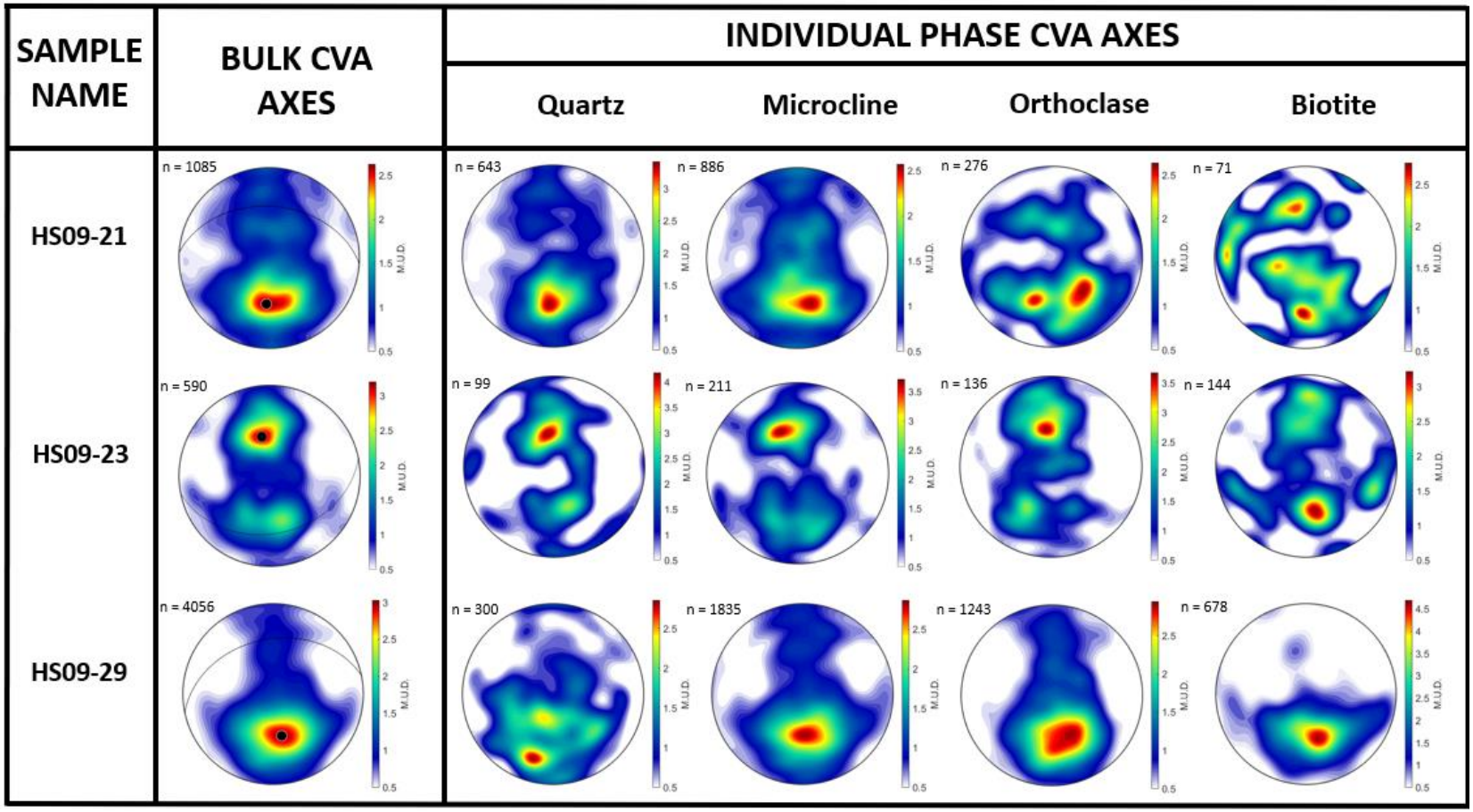

Figure 24: Lower hemisphere, equal area projections showing phase specific crystallographic vorticity axis. Black dot indicates the orientation of the bulk vorticity axis (on left), black great circle represents the orientation of the vorticity normal surface. Plots are color contoured (multiples of uniform density, M.U.D.), with a 10-degree halfwidth, representing the corresponding orientation distribution function for each set of orientations. N represents number of grain-scale axes analyzed.

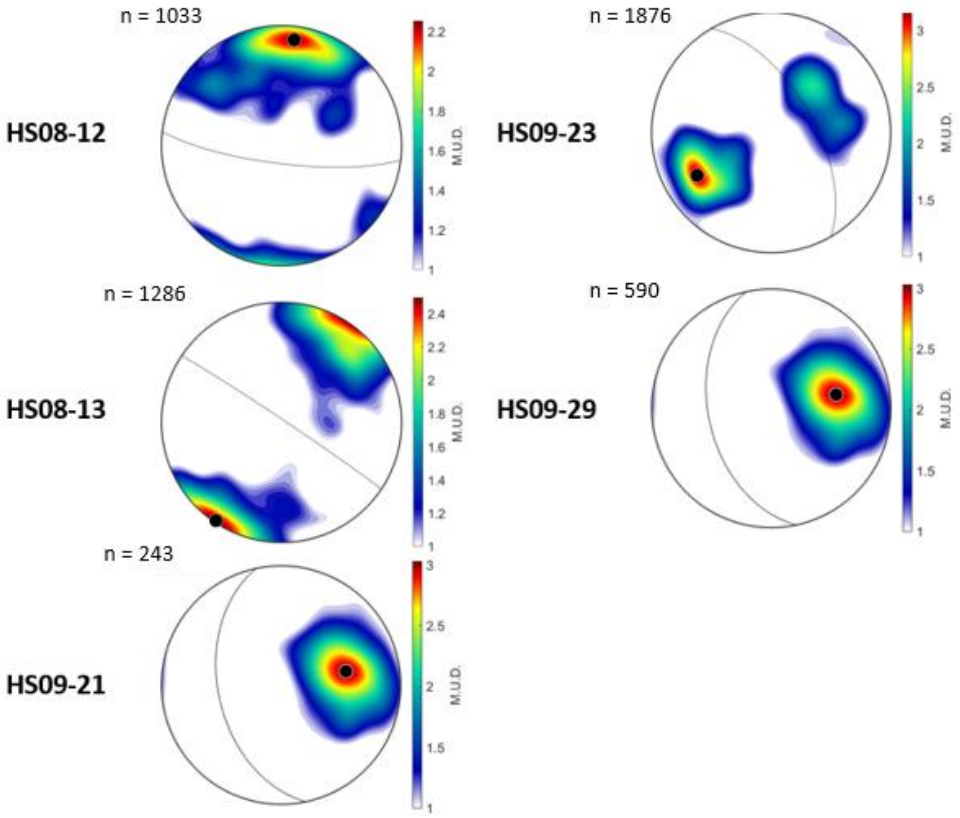

Figure 25: Rotated CVA plots shown in the geographic reference frame using fabric foliation and stretching lineation orientations. Black dot indicates the orientation of the bulk vorticity axis (on left), black great circle represents the orientation of the vorticity normal surface.

CHAPTER 5: DISCUSSION

5.1 Deformation Temperatures and Quartz Crystallographic Preferred Orientation Plots

Quartz recrystallization microstructures and CPOs can be used to infer deformation mechanisms and temperature estimates (Hirth and Tullis, 1992; Stipp et al., 2002b). The HSZ contains a pervasive foliation that strikes northeast and dips steeply to the southeast. In the HSZ samples, mica fish and a steep, quartz oblique grain-shape fabric in quartz indicate top-up-to-the-northwest shear sense. Deformation in the Holy Cross City (HSZ, samples HS08-12 and 13) occurred at temperatures between 400-500°C based on the presence of SGR quartz (Figures 15 and 16). In the SLSZ mylonite, mineral assemblages, shear-sense indicators, and deformation temperatures are more variable and distinctive compared to HSZ samples. Based on the recrystallization textures in samples from the SLSZ, along with what was reported by Lee et al. (2012), the SLSZ is relatively higher strain than the HSZ. SLSZ mylonites contain a variety of kinematic indicators with some samples displaying mica fish, S-C' fabrics, relict sillimanite porphyroclasts, and oblique grain-shape fabrics. Sample SL08-04 is a quartz mylonite vein from the Homestake Peak splay of the SLSZ, characterized by a steep oblique grain-shape fabric of SGR and GBM quartz (450–550°C) exhibiting top-down-to-the-southeast shear sense. The Slide Lake Cirque splay samples (SLSZ, samples HS09-21,23,29) contain less quartz than SL08-04. All three samples contain retrograde sericite or muscovite that record greenschist facies conditions that overprint higher temperature features. Sillimanite is present in samples HS09-23 and 29 along with local domains of GBAR quartz that

reflects Paleoproterozoic, high temperature melt-present flow (D_1). Shear-sense indicators exhibit top-down-to-the-southeast shear sense. Lee et al. (2012) observed top-up-to-the-northwest sense of shear for sample HS09-29, although that was not observed in this research. SLSZ samples record a variety of temperatures, an earlier, high temperature (600°C) event is recorded by sillimanite and GBAR quartz. A post D_1, moderate temperature (400–500°C) event is recorded by greenschist facies mineral assemblages and SGR quartz.

Quartz c- and a-axis pole figures for samples from the HSZ agree with what was reported by Lee et al. (2012). Deformation in the Holy Cross City Splay HSZ is dominated by prism <a> with a component of rhomb <a> slip under plane strain conditions. Deformation temperature estimates determined from quartz CPO plots are in the range of 500–650°C. Temperature estimates determined from quartz recrystallization textures are slightly lower. This variation could be a result of the EBSD measurements derived from a smaller, higher-strain domain within the sample. Sample HS08-12 and 13 photomicrographs (Figure 15 and 16) cover a larger area than the EBSD analyzed region and are more representative of the sample.

The SLSZ samples contain a much larger variation in CPO patterns. Quartz CPO patterns are indicative of prism <a> slip (SL08-04, HS09-21,29) and possibly prism <c> slip (HS09-23). Slip-system activity in SL08-04 is consistent with what was reported by Lee et al. (2012); this sample is characterized by prism <a> and a minor rhomb <a> slip component. The CPO pattern (Figure 21) from this research doesn't match what was recorded by Lee et al. (2012) (Figure 12C). This variation could be due to differences in

the region analyzed by EBSD. Nonetheless, both patterns indicate the same slip systems were active. CPO patterns from samples HS09-21 and HS09-29 are weaker compared to other SLSZ samples. This is likely due to the abundance of other phases that are controlling deformation within the SLSZ. Sample HS09-23 exhibits a prominent CPO pattern that plots approximately normal to the YZ plane of deformation fabric, that is the CPO is parallel to the lineation direction. This pattern indicates prism <c> slip, suggesting deformation occurred at high temperatures (>650 °C). Temperature estimates from quartz CPO patterns for sample HS09-23 are consistent with temperature estimates recorded by GBAR and the presence of sillimanite.

In agreement with Lee et al. (2012), the quartz CPO patterns, and deformation temperature estimates support the model that the HSZ and SLSZ are likely developed at similar crustal levels in a similar tectonic setting. The kinematic data presented indicate a similarity between the meso- and microscale deformation mechanisms and temperatures in the SLSZ and HSZ. Results from CVA analysis were used to determine the orientation of the bulk vorticity axis and vorticity normal surface during the last increment of deformation.

5.2 Crystallographic Vorticity Axis Analysis

The kinematic reference frame cannot reliably be based on fabric relationships. Kinematic interpretations are most accurately determined within the vorticity normal plane, which does not always align with the XZ plane. CVA analysis is a new method of determining the bulk vorticity axis and corresponding vorticity normal surface orientation. Results of CVA analysis can be used to reevaluate previously established

deformation and kinematic models. The results of CVA analysis are distinctive for the HSZ and SLSZ (Figure 23). For the HSZ, results indicate that the bulk vorticity axis is vertical, plotting within the plane of foliation. This particular pattern is consistent with the vorticity axis expected for simple shear and wrench-dominated, dextral transpression involving general shear (Figure 2: Tikoff et al., 2013; Michels et al., 2015; Kruckenberg et al., 2019). Based on these results, the HSZ exhibits a monoclinic shear-zone geometry. These data support the model proposed by Lee et al., (2012) that the HSZ formed because of widening-thinning (e.g., transpression) shear. The results from CVA analysis for HSZ samples indicate that accurate kinematic interpretations can be made from viewing samples in the XZ plane. The rotated CVA plots reveal the vorticity axis plotting along the perimeter, and the vorticity-normal surface striking through the center of the plot.

CVA analysis results for samples from the SLSZ are more variable and ambiguous. For sample SL08-04, the vorticity normal surface, presented on an equal area stereographic projection (Figure 23), is oriented striking southwest. The vorticity vector is plunging moderately to the southeast, oblique to the foliation plane. Despite being collected in the same approximate area, samples HS09-21 and -29 show different orientations for the vorticity vector than sample HS09-23. Sample HS09-21 and -29 are consistent with the vorticity normal surface striking to the west, and the vorticity vector moderately plunging to the south. The vorticity normal surface for sample HS09-23 strikes to the east, with the vorticity vector plunging moderately to the north. In all four SLSZ samples, the vorticity vector plots oblique to the foliation plane. This pattern is not consistent with the geometry expected of monoclinic shear zones and illustrates the

possibility of the SLSZ exhibiting a component of triclinic transpression (Figure 2). The rotated CVA plots for samples HS09-21, -23, and -29 (Figure 25) contain the same variation as the specimen reference frame CVA plots (Figure 23). Sample HS09-23 shows the inverse pattern of HS09-21, and -29. This is unexpected considering the similarity in the samples but could be related to the nature of heterogenous shear zones. Mylonite from the Slide Lake Cirque splay of the SLSZ contain a variety of phases, with feldspar and quartz being the most abundant. CVA was applied to individual phases within these samples, and the results show the contributions of each phase to the bulk vorticity axis. All three samples (Figure 24) show that microcline appears to be the dominant phase controlling the orientation of the bulk vorticity axis. Therefore, future studies of this shear zone splay should focus on the rheology of feldspar in conjunction with quartz. This application of phase specific CVA analysis is insightful given the current understanding of large-scale, mid-crustal shear zones.

Based on the CVA plots for the SLSZ samples, kinematic interpretations would be most accurately interpreted in the vorticity normal plane, which, in these samples, does not coincide with the common kinematic reference frame. Therefore, the current SLSZ samples should be used with caution when evaluating kinematics. Accurate kinematic interpretations could be made from properly cut thin sections or EBSD data that were rotated to plot within the vorticity-normal surface for the SLSZ samples. One explanation for the difference in deformation geometries could be that the HSZ and SLSZ were active during different deformation events, but the meso- and microscale similarities suggest they were active at similar crustal levels and a similar tectonic regime (Lee et al.,

2012). To my current knowledge, only one study (Leierzapf, MS Thesis 2019) has focused on the timing of deformation within the SLSZ. Their research used monazite geochronology to estimate timing of deformation within the two shear zones. Their results indicate that the two shear zones were active at the same time throughout the Middle Proterozoic. One potential explanation for the difference in shear zone geometries, given the similarity in deformation conditions, is that the two shear zones were active at different times with ages potentially falling within the margin of error for monazite geochronology. It should also be noted that the difference in vorticity vector orientations for the SLSZ samples could be attributed to sample viability, as sample HS09-23 comprised a much smaller mapped area compared to HS09-21 and -29 and the number of grain orientations used varied for each sample.

5.3 Low-Angle Intragranular Boundary Misorientations

Plots produced from low-angle, intragranular misorientation axis analysis indicate that quartz deformation within the Holy Cross City splay of the HSZ was dominated by prism <a> slip. Results from this method (Figure 22) are consistent with the slip system analysis results from quartz CPO plots (Figure 21) and the results reported by Lee et al. (2012). Sample HS08-12 contains a dominant prism <a> slip component. Sample HS08-13 reveals a dominant prism <a> slip component, and a weak distribution around the [01-10] axis indicating a minor rhomb <a> or basal <a> component of slip. Although the results are consistent with quartz CPO plots, the results from HS08-12 and HS08-13 should be interpreted with caution because of a small number of orientations (N= 47 and N = 54, respectively). The small number of low-angle grain boundary orientations are

likely a product of deformation, as these samples contain a steep, oblique grain-shape foliation. The CPO plots reflect crystal lattice-scale preferred orientations, while the low-angle intragranular misorientation analysis method reflect low-angle, grain boundary orientations. Using this method, grains oriented at a high angle to foliation may not yield orientations that are suitable for analysis, resulting in a smaller orientation size (N). Additionally, this method inherently uses fewer orientations to estimate slip system activity. Data for the SLSZ samples indicate predominant prism <a> and basal or rhomb <a> slip. The plots for SL08-04 and HS09-21 match the corresponding CPO data: a strong maximum around the [0001] axis. CPO plots for sample HS09-23 display evidence of high-temperature, prism <c> slip, but, the plot from this method does not agree with that result. This variation is likely due to a small number of low-angle, intragranular misorientations (N = 11). The CPO likely reflects a more accurate record of deformation for sample HS09-23. This approach offers a novel way of evaluating previously published slip-system analysis results.

CHAPTER 6: CONCLUSION

1) Proterozoic age shear zones in central Colorado record a complex sequence of deformation events associated with the growth of Laurentia. In the Colorado mineral belt, the HSZ is a steeply dipping, northeast striking ductile shear zone that has been heavily studied as one of the fundamental structures that controlled Laramide age plutonism and associated ore deposits. Exposed 4 km to the south, the less studied, shallowly dipping, northeast striking SLSZ exposes a variety of complexly deformed mylonite, ultramylonite, and migmatite. These shear zones offer a natural laboratory to apply modern vorticity and kinematic techniques to better understand shear zone processes in the middle crust. Six previously collected samples were chosen to investigate kinematic vorticity and constrain deformation conditions within the HSZ and SLSZ.

2) Crystallographic vorticity axis analysis and slip system analysis was applied to all samples to determine the orientation of the bulk vorticity vector and to evaluate which slip systems were active in quartz during deformation. This study documents the SLSZ as having a distinct deformation geometry from the neighboring HSZ. Deformation conditions for both shear zones are consistent with previous research (Lee et al., 2012). Deformation in the HSZ involved several episodes of reactivation, recorded by SGR and GBM quartz and rhomb <a> slip system activity in quartz. The orientation of the vorticity vector for the HSZ is in the plane of foliation, corresponding to a vertical vorticity vector indicating the HSZ exhibits a monoclinic shear zone geometry characterized by wrench-dominated, dextral transpression. The SLSZ is characterized by mylonites and ultramylonites exhibiting high temperature deformation textures (SGR to GBAR, 450 to

>650°C) and greenschist to amphibolite facies mineral assemblages. New EBSD data for the SLSZ confirm the published data by Lee et al. (2012), indicating dominant prism <a> slip to rhomb <a> slip, with one sample recording prism <c> slip.

3) Low angle, intragranular misorientation analysis reveals dominant prism <a> slip and rhomb <a> to basal <a> slip in all samples. Results from crystallographic vorticity axis analysis of SLSZ samples are not as straightforward as they are for the HSZ. This research documents that the SLSZ likely exhibits a triclinic shear zone geometry based on the orientation of the vorticity vector, which is parallel to the plane of foliation and lineation. The kinematic model proposed by Lee et al. (2012) appears to be accurate for the HSZ, and we agree that deformation within the HSZ was associated with reshuffling of blocks during transpression to accommodate strain along the margin of Laurentia.

4) Additionally, this research shows that phase specific CVA vectors are consistent with the bulk CVA vector, illustrating that CVA analysis can be applied to a wide range of mineralogies, not only quartz. The kinematics of the SLSZ samples presented in Lee et al. (2012) and this study should be interpreted with caution since the vorticity normal section does not lie within the XZ plane.

CHAPTER 7: FUTURE WORK

This research indicates that the HSZ and SLSZ exhibit different deformation geometries. We utilized existing and newly acquired EBSD data to constrain the orientation of the vorticity vector for six samples from the HSZ and SLSZ. Although we are confident in our data, more EBSD data needs to be collected on a variety of samples from different portions of the shear zones. The existing thin section suite should be polished in a manner that allows for EBSD analysis, as many of the thin sections have cover slips. A larger sample size would be beneficial, allowing for the orientation of the bulk vorticity axis to be better constrained across the broad shear system. In conjunction with more EBSD analysis, several methods exist to further constrain the history of the SLSZ and HSZ. The oblique grain shape (OGS) method could be applied to samples containing an oblique grain shape in quartz. This would allow for the calculation of the kinematic vorticity number. The OGS method also allows for the determination of flow apophyses and instantaneous stretching axes, which are useful in evaluating paleoconvergence vectors. A higher resolution EBSD data set would allow for more accurate grain reconstruction, which can be used to calculate the amount of quartz recrystallization within a sample. Consequently, the quartz recrystallized grain size piezometer (Stipp and Tullis, 2003) could be applied to evaluate paleostress within the two shear zones, this would offer another way of examining the conditions (stress and depth) under which strain localization occurred. With a more robust data set, research within the CMB will continue to evolve and provide a clearer picture of processes in the middle crust throughout the Proterozoic.

REFERENCES

Allen, J.L., 2005. A multi-kilometer pseudotachylyte system as an exhumed record of earthquake rupture geometry at hypocentral depths (Colorado, USA): Tectonophysics, V. 402, No. 1-4, pp. 37-54.

Allen, J.L., O'Hara, K.D., and Moecher, D.P., 2002. Structural geometry and thermal history of pseudotachylyte from the Homestake shear zone, Sawatch Range, Colorado: Geological Society of America Field Guides, V. 3, pp. 17-32.

Allen, J.L., and Shaw, C.A., 2013. Seismogenic fault-zone processes and heterogeneity recorded by pseudotachylyte: New insights from the Homestake shear zone, Colorado: Geological Society of America Field Guides, V. 33, pp. 165-183.

Bennett, V. C., and DePaolo, D. J., 1987, Proterozoic crustal history of the western United States as determined by neodymium isotopic mapping: Geological Society of America Bulletin, V. 99, pp. 674–685.

Behrmann, J.H., and Mainprice, D., 1987. Deformation mechanisms in a high-temperature quartz – feldspar mylonite: evidence for superplastic flow in the lower continental crust: Tectonophysics, V. 150, pp. 297-305.

Bickford, M.E., and Hill, B.M., 2007. Does the arc accretion model adequately explain the Paleoproterozoic evolution of southern Laurentia? An expanded interpretation: Geology, V. 35, No. 2, pp. 167-170.

Bowring, S.A., and Karlstrom, K.E., 1990. Growth, stabilization, and reactivation of Proterozoic lithosphere in the southwestern United States: Geology, V. 18, pp. 1203-1206.

Condie, K. C., 1986, Geochemistry and tectonic setting of early Proterozoic supracrustal rocks in the southwestern United States: Journal of Geology, V. 94, pp. 845–864.

Darbyshire, F. A., Bastow, I.D., Petrescu, L., Gilligan, A., and Thompson, D.A., 2017. A tale of two orogens: Crustal processes in the Proterozoic Trans-Hudson and Grenville Orogens, eastern Canada: Tectonics, V. 36, pp. 1633–1659,

Diaz-Azpiroz, M., Fernandez, C., and Czeck, D.M., 2018. Are we studying deformed rocks in the right sections? Best practices in the kinematic analysis of 3D deformation zones: Journal of Structural Geology, V.125, pp. 218-225.

Duebendorfer, E.M., Chamberlain, K.R., and Jones, C.S., 1987. Paleoproterozoic tectonic history of the Cerbat Mountains, northwestern Arizona: Implications for crustal

assembly of the southwestern United States: GSA Bulletin, V. 113, No. 5, pp. 575-590.

Duebendorfer, E.M., and Christenson, C., 1995. Synkinematic (?) intrusion of the "anorogenic" 1425 Ma Beer Bottle Pass pluton, southern Nevada: Tectonics, V. 14, No. 1, pp. 168-184

Flynn, C., 2021. Vorticity and Kinematic Analysis of the Cordillera Blanca Shear Zone, Peru. Master's Thesis, University of Tennessee, 2021.

Fossen, H., and Cavalcante, G.C., 2017, Shear zones - a review: Earth-Science Reviews, V. 171, pp. 435-455, doi: https://doi.org/10.1016/j.earscireV.2017.05.002

Giorgis, S., Michels, Z., Dair, L., Braudy, N., and Tikoff, B., 2016. Kinematic and vorticity analyses of the Western Idaho shear zone, USA: Lithosphere, V. 9, No. 2, pp. 223-234.

Hamilton, W., 1981. Crustal evolution by arc magmatism. Philosophical Transactions of the Royal Society of London. Series A, Mathematical and Physical Sciences, V. 301, pp. 279-291.

Hirth, G., and Tullis, J., 1992. Dislocation creep regimes in quartz aggregates. Journal of Structural Geology, V. 14(2), pp. 145–159.

Hirth, G., Teyssier, C., and Dunlap, W.J., 2001. An evaluation of quartzite flow laws based on comparisons between experimentally and naturally deformed rocks: International Journal of Earth Sciences, V. 90, pp. 77-87.

Hoffman, P.F., UNITED PLATES OF AMERICA, THE BIRTH OF A CRATON: Early Proterozoic Assembly and Growth of Laurentia: Annual Reviews of Earth and Planetary Sciences, V. 16. Pp.543-603.

Jessup, M.J., Karlstrom, K.E., Connelly, J., Williams, M., Livaccari, R., Tyson, A., and Rogers, S.A., 2005. Complex Proterozoic crustal assembly of southwestern North America in an arcuate subduction system: the Black Canyon of the Gunnison, southwestern Colorado: The Rocky Mountain Region - An Evolving Lithosphere. American Geophysical Union Monograph, V. 154, pp. 1-19.

Jessup, M.J., Jones III, J.V., Karlstrom, K.E., Williams, M.L., Connelly, J.NO., Heizler, M.T., 2006. Three Proterozoic orogenic episodes and an intervening exhumation event in the Black Canyon of the Gunnison region, Colorado: Journal of Geology, V. 114, pp. 555-576.

Jessup, M.J., Law, R.D., and Frassi, C., 2007. The Rigid Grain Net (RGN): An alternative method for estimating mean kinematic vorticity number (Wm): Journal of Structural Geology, V. 29, pp. 411-421.

Jones III, J.V., Rogers, S.A., Connelly, J.NO., 2010a, U-Pb geochronology of Proterozoic granites in the Sawatch Range, central Colorado, U.S.A.: Rocky Mountain Geology V. 45, pp. 1-22.

Karlstrom, K. E., and Bowring, S. A., 1988, Early Proterozoic assembly of tectonostratigraphic terranes in southwestern North America: Journal of Geology , V. 96, pp. 561–576.

Karlstrom, K.E., and Houston, R.S., 1984. The Cheyenne Belt: Analysis of a Proterozoic suture in southern Wyoming: Precambrian Research, V. 25, No. 4, pp. 415-446.

Karlstrom, K.E., and Humphreys, E.D., 1998. Persistent influence of Proterozoic accretionary boundaries in the tectonic evolution of southwestern North America: Interaction of cratonic grain and mantle modification events: Rocky Mountain Geology, V. 33, No. 2, pp. 161-179.

Kruckenberg, S.C., Michels, Z.D., and Parsons, M.M., 2019. From intracrystalline distortion to plate motion: Unifying structural, kinematic, and textural analysis in heterogeneous shear zones through crystallographic orientation-dispersion methods: Geosphere, V. 15, No. 2., pp. 357-381.

Law, R.D., 1990. Crystallographic fabrics: a selective review of their applications to research in structural geology: Geological Society Special Publication, No. 54, pp. 335-352.

Law, R.D., Casey, M., Knipe, R.J., 1986. Kinematic and tectonic significance of microstructures and crystallographic fabrics within quartz mylonites from the Assynt and Eriboll regions of the Moine thrust zone, NW Scotland. Transactions of the Royal Society of Edinburgh: Earth Sciences, V. 77, pp. 99-126.

Law, R.D., Knipe, R.J., Dayan, H., 1984. Strain-path partitioning within thrust sheets: microstructural and petrofabric evidence from the Moine thrust zone at Loch Eriboll, northwest Scotland: Journal of Structural Geology, V. 6, pp. 477-497.

Langille, J.M., Jessup, M.J., Cottle, J.M., Newell, D., and Serward, G., 2010. Kinematic evolution of the Ama Drime detachment: Insights into orogen-parallel extension and exhumation of the Ama Drime Massif, Tibet-Nepal: Journal of Structural Geology, V. 32, i. 7, pp. 900-919.

Lee, E.P., Jessup, M.J., Shaw, C.A., Hicks, G.L., and Allen, J.L., 2012. Strain partitioning in the mid-crust of a transpressional shear zone system: Insights from the Homestake and Slide Lake shear zones, central Colorado: Journal of Structural Geology, V. 39, pp. 237-252.

Leierzapf, J., 2020, Electron microprobe in situ monazite dating of the Slide Lake shear zone [M.S. thesis]: The University of Tennessee, Knoxville, 105 pp.

Lu, L.X., and Jiang, D., 2018. Quartz Flow Law Revisited: The Significance of Pressure Dependence of the Activation Enthalpy: Journal of Geophysical Research: Solid Earth, V. 124, pp. 241-256.

McCoy, A.M., Karlstrom, K.E, Shaw, C.A., and Williams, M.L., 2005. The Proterozoic Ancestry of the Colorado Mineral Belt: 1.4 Ga Shear Zone System in Central Colorado: The Rocky Mountain Region: An Evolving Lithosphere, American Geophysical Union Monograph, V. 154, pp. 71-90.

Means, W.D., Hobbs, B.E., Lister, G.S., and Williams, PP.F., 1980. Vorticity and non-coaxiality in progressive deformation: Journal of Structural Geology, V. 2, No. 3, pp. 371-378.

Michels, Z.D., 2021. GitHub – zmichels/Fabrica. GitHub.com. https://github.com/zmichels/Fabrica. Accessed: December 2021

Michels, Z.D., 2021. GitHub – zmichels/misorientationss. GitHub.com. https://github.com/zmichels/misorientations. Accessed: December 2021.

Michels, Z.D., Kruckenberg, S.C., Davis, J.R., and Tikoff, B., 2015. Determining vorticity axes from grain-scale dispersion of crystallographic orientations: Geology, V. 43, No. 9, pp. 803-806.

Molnar, P., Continental tectonics in the aftermath of plate tectonics: Nature, V. 335, pp. 131-137.

Nie, G., and Shan, Y., 2014. Development of quartz c-axis crossed/single girdles under simple-pure shear deformation: Results of visco-plastic self-consistent modeling: Journal of Structural Geology, V. 66, pp. 261-270.

Nyman, M.W., Karlstrom, K.E., Kirby, E., and Graubard, C.M., 1994. Mesoproterozoic contractional orogeny in western North America: Evidence from ca. 1.4 Ga plutons: Geology, V. 22, pp. 901-904.

Oxford Instruments, 2015, EBSD Explained - From data acquisition to advanced analysis. https://nano.oxinst.com/products/ebsd/?19_form_success=1. (Accessed, May 2021).

Passchier, C.W., 1998. Monoclinic model shear zones: Journal of Structural Geology, V. 20, No. 8, pp. 1121 to 1137.

Passchier, C.W., Trouw, R.A.J., 2005. Microtectonics, second ed. Springer, Berlin, 366 pp. 289.

Passchier, C.W., and Urai, J.L., 1988. Vorticity and strain analysis using Mohr diagrams: Journal of Structural Geology, V. 10, No. 7, pp. 755-763.

Pennacchioni, G., Menegon, L., Leiss, B., Nestola, F., and Bromiley, G., 2010. Development of crystallographic preferred orientation and microstructure during plastic deformation of natural coarse-grained quartz veins: Journal of Geophysical Research, V. 115, No. B12.

Platt, J.PP., and Berhmann, J.H., 1986. Structures and fabrics in a crustal-scale shear zone, Betic Cordillera, SE Spain: Journal of Structural Geology, V. 8, No. 1, pp. 15-33.

Ramsay, J.G., and Graham, R.H., 1970, Strain variation in shear belts: Canadian Journal of Earth Sciences, V. 7, pp. 786-813. doi: https://doi.org/10.1139/e70-078.

Robin, PP.F., and Cruden, A.R., 1994. Strain and vorticity patterns in ideally ductile transpression zones: Journal of Structural Geology, V. 16, No. 4 pp. 447 to 466.

Schmidt, K.L., Lewis, R.S., Vervoort, J.D., Stetson-Lee, T.A., Michels, Z.D., and Tikoff, B., 2017. Tectonic evolution of the Syringa embayment in the central North American Cordilleran accretionary boundary: Lithosphere, V. 9m No. 2, pp. 184-204.

Selverstone J., Hodgins, M., Aleinikoff, J.NO., and Fanning, C.M., 2000. Mesoproterozoic reactivation of Paleoproterozoic transcurrent boundary in the northern Colorado Front Range: Implications for ~1.7- and 1.4-Ga tectonism: Rocky Mountain Geology, V. 35, No. 2, pp. 139-162.

Shaw, C.A., Allen, J.L., 2007. Field rheology and structural evolution of the Homestake shear zone, Colorado: Rocky Mountain Geology 42, 31e56.

Shaw, C.A., and Karlstrom, K.E., 1999. The Yavapai-Mazatzal crustal boundary in the Southern Rocky Mountains: Rocky Mountain Geology, V. 34, No. 1, pp. 37-52.

Shaw, C.A., Karlstrom, K.E., Williams, M.L., Jercinovic, M.J., and McCoy, A.M., 2001. Electron-microprobe monazite dating of ca. 1.71-1.63 Ga and ca. 1.45-1.38 Ga deformation in the Homestake shear zone, Colorado: Origin and early evolution of a persistent intracontinental tectonic zone: Geology, V. 29, No. 8, pp. 739-742.

Simpson C., De Paor D.G., 1997. Practical analysis of general shear zones using the porphyroclast hyperbolic distribution method: An Example from the Scandinavian Caledonides: Sengupta S. (eds) Evolution of Geological Structures in Micro- to Macro-scales. Springer, Dordrecht.

Stipp, M., Stünitz, H., Heilbronner, R., Schmid, S.M., 2002b. Dynamic recrystallization of quartz: correlation between natural and experimental conditions. In: DeMeer, S., Brury, M.R., De Brasser, J.H.PP., Pennock, G.M. (Eds.), Deformation Mechanisms, Rheology and Tectonics: Current Status and Future Perspectives. Geological Society, London, Special Publication, vol. 200, pp. 171e190.

Stipp, M., and Tullis, J., 2003. The recrystallized grain size piezometer for quartz. Geophysical Research Letters, V. 30, No. 21.

Tikoff, B., and Greene, D., 1997. Stretching lineations in transpressional shear zones: an example from the Sierra Nevada Batholith, California: Journal of Structural Geology, V. 19, No. 1, pp. 29 – 39.

Tikoff, B., and Fossen, H., 1995. The limitations of three-dimensional kinematic vorticity analysis: Journal of Structural Geology, V. 17, No. 12, pp. 1771-1784.

Tikoff, B., and Teyssier, C., 1994. Strain modeling of displacement-field partitioning in transpressional orogens: Journal of Structural Geology, V. 16, No. 11, pp. 1575 to 1588.

Truesdell, C., 1953. Two measures of vorticity: Journal of Rotational Mechanics Analysis, V. 2, pp. 173-217.

Tullis, J., and Yund, R.A., 1977. Experimental deformation of dry westerly granite: Journal of Geophysical Research, V. 82, No. 36, pp. 5705 – 5718.

Tullis, J., and Yund, R.A., 1987. Transition from cataclastic flow to dislocation creep of feldspar: Mechanisms and microstructures: Geology, V. 15, pp. 606-609.

Tweto, O., 1974, Geologic map and sections of the Holy Cross Quadrangle, Eagle, Lake, Pitkin, and Summit Counties, Colorado: U.S. Geological Survey Miscellaneous Investigations Map I-830, scale 1:24 000.

Tweto, O., 1979. Geologic Map of Colorado. United States Geological Survey, scale 1:500,000.

Tweto, O., and Sims, PP.K., 1963. Precambrian Ancestry of the Colorado Mineral Belt: Geological Society of America Bulletin, V. 74, pp. 991-1014.

Wallis, S.R., 1992. Vorticity analysis in a metachert from the Sanbagawa belt, SW Japan: Journal of Structural Geology, V. 14, No. 4, pp. 271-280.

Wilson, C. J.L., 1975. Preferred Orientation in Quartz Ribbon Mylonites: Geological Society of America Bulletin, V. 86, pp. 968-974.

Xypolias, PP., 2010. Vorticity analysis in shear zones: A review of methods and applications: Journal of Structural Geology, V. 32, pp. 2072-2092.

APPENDICES

APPENDIX I: MATLAB Scripts

Import the EBSD Data. Apply relevant rotation to match SEM images and pole figures. Filter out any irrelevant phases such as non-indexed grains. MATLAB scripts were modified from the MTEX Github and the CVA and misorientations repositories on GitHub.

All Quartz Orientations Pole Figure

```
oq = ebsd('Quartz').orientations; %% THIS COMPUTES ALL
QUARTZ ORIENTATIONS POLE PLOT
cs = oq.CS;
h= [Miller(0,0,0,1,'uvtw',cs),Miller(1,1,-
2,0,'direction',cs),Miller(1,0,-1,0,'direction',cs)];
figure,
plotPDF(oq,h,'lower','points','all','MarkerSize',1)
annotation('textbox',[0 .7 0 .3],'String',sprintf('n =
%i',length(ebsd('Quartz'))),'FitBoxToText','on');
```

Contoured Pole Figure

```
%% Compute an ODF
odf = calcDensity(oq,'haldwidth',10*degree);
%% plot the ODF as a pole figure
figure,
plotPDF(odf,h,'antipodal','lower','smooth','halfwidth',15*d
egree,'colorrange','equal')
cb = mtexColorbar('Title','M.U.D.');
cb.Limits = [1 cb.Limits(2)];
annotation('textbox',[0 .7 0 .3],'String',sprintf('n =
%i',length(oq)),'FitBoxToText','on')
```

Grain Reconstruction, required for CVA

```
%% reconstruct grain boundaries
lagb = 2*degree;
hagb = 10*degree;
[grains,ebsd.grainId,ebsd.mis2mean] =
calcGrains(ebsd,'angle','tight',[hagb lagb]);
```

```
%% Filter the grain set
% by number of included solutions
grains = grains(grains.grainSize>=3);

%% Reconstructed Grain Boundary Map
% reset the ebsd variable
ebsd = ebsd (grains);
% recompute grain boundaries;
[grains,ebsd.grainId,ebsd.mis2mean] =
calcGrains(ebsd,'angle','tight',[hagb lagb]);
grains = smooth(grains,5,'moveTriplePoints');
```

Contoured Pole Figure for mean grain orientations for Quartz, uses grain reconstruction from previous step

```
o = grains('Quartz').meanOrientation;
figure,
plotPDF(o,h,'antipodal','lower','smooth','halfwidth',10*deg
ree,'colorrange','equal')

cb = mtexColorbar('Title','M.U.D.');
cb.Limits = [1 cb.Limits(2)];

%% Compute an ODF
odf = calcDensity(o,'haldwidth',10*degree);
% plot the ODF as a pole figure
figure,
plotPDF(odf,h,'antipodal','lower','smooth','colorrange','eq
ual')
cb = mtexColorbar('Title','M.U.D.');
cb.Limits = [1 cb.Limits(2)];
annotation('textbox',[0 .7 0 .3],'String',sprintf('n =
%i',length(o)),'FitBoxToText','on')
```

Code for CVA Analysis

```
[gCVA,bv] = grainsCVA(grains,ebsd);
% %
% %
% % Make a plot of the CVA results and add the bulk CVA
vector
figure,
plot(gCVA.CVA,'antipodal','lower','smooth','halfwidth',10*d
egree)
hold on
```

```
plot(bv,'antipodal'',lower','Marker','o','MarkerSize',15,'M
arkerFaceColor','k','MarkerEdgeColor','w')
plot(bv,'plane')
cb = mtexColorbar('Title','M.U.D.');
setColorRange([.5 max(cb.Limits)])
annotation('textbox',[0 .7 0 .3],'String',sprintf('n =
%i',length(gCVA)),'FitBoxToText','on')

% %
% figure, %%individual, phase specific cva

%
plot(gCVA('Orthoclase').CVA,'antipodal','lower','smooth','h
alfwidth',10*degree)
% annotation('textbox',[0 .7 0 .3],'String',sprintf('n =
%i',length(gCVA('Orthoclase'))),'FitBoxToText','on')
% cb = mtexColorbar('Title','M.U.D.')
% setColorRange([.5 max(cb.Limits)])
```

Rotating CVA

```
strike = ##;
dip = ##;
trend = ##;
plunge = ##;
%% use geoFab()
linDir = -vector3d.X;
poleDir = vector3d.Y;
[fabOr, fabRot, strikeV, poleV, linV] =
geoFab(strike,dip,trend,linDir,poleDir);
%% Use the variable 'fabRot' to rotate any data...
% can be used to rotate CVA or CPO plots
% all cva vectors
cva = gCVA.CVA;
[~,bulkCVA] = max(calcDensity(cva));
% apply the rotation
cvaRot = fabRot*cva;
bulkCVARot = fabRot*bulkCVA;

figure,
plot(cvaRot,'antipodal','lower','smooth','halfwidth',10*deg
ree,'figsize','large');
cb = mtexColorbar('Title','M.U.D.');
setColorRange([1 max(cb.Limits)]);
hold on
```

```
plot(bulkCVARot,'antipodal'',lower','Marker','o','MarkerSiz
e',15,'MarkerFaceColor','k','MarkerEdgeColor','w')
plot(bulkCVARot,'plane')
annotation('textbox',[0 .7 0 .3],'String',sprintf('n =
%i',length(gCVA)),'FitBoxToText','on')
hold off
%% trend and plunge of the rotated CVA data
% all the CVA
[trend_CVA,plunge_CVA]=V2TP(cvaRot);
trend_CVA = trend_CVA(:);
plunge_CVA = plunge_CVA(:);
% bulk CVA
[trend_bulkCVA,plunge_bulkCVA]=V2TP(bulkCVARot);
```

Low Angle Intragranular Misorientation Analysis

```
%% low-angle boundary misorientation analysis

% get all the subgrain/inner boundaries from the grainset
subB = grains('Quartz').innerBoundary;
subB
% % boundaries of the phase of interest (forsterite in our
example case)


% % condition for only misorientations with angles of
certain threshold (can define below)
% plotAngleDistribution(subB)
condLAB = subB.misorientation.angle>=1*degree &
subB.misorientation.angle<#*degree;
% % % the "low-angle" boundaries of interest
labQ = subB(condLAB);
labQ
% % plot crystal reference frame
figure,
plotAxisDistribution(labQ.misorientation,'antipodal','lower
','smooth','halfwidth',15*degree,'figSize','small')
mtexColorbar('Title','M.U.D.');
% setColorRange([0 max(cb.Limits)]);
annotation('textbox',[0 .7 0 .3],'String',sprintf('n =
%i',length(labQ)),'FitBoxToText','on');
```

APPENDIX II: Sample Data

Structural Relationships:

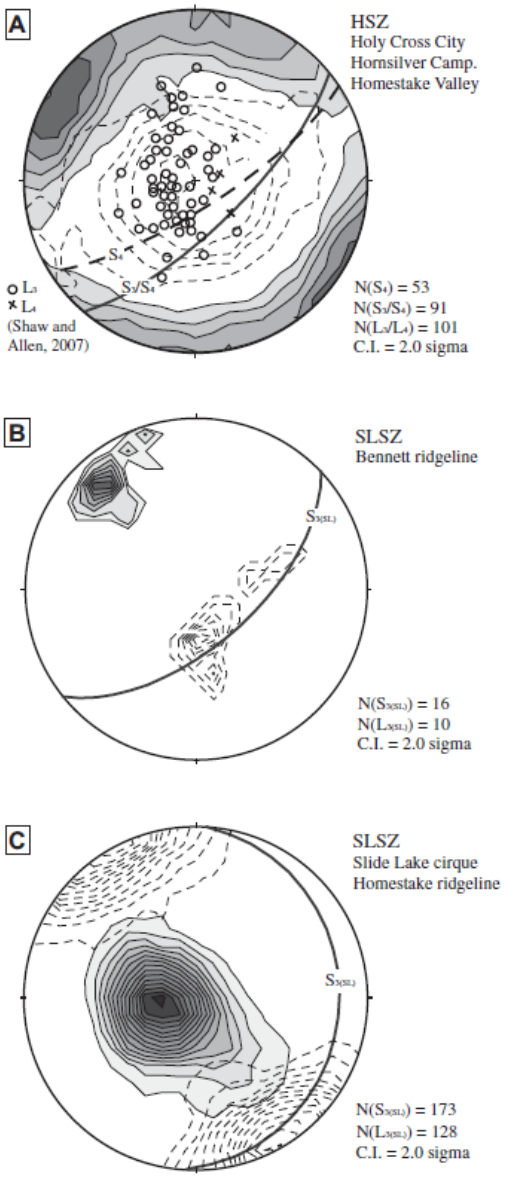

Figure Description: Lower hemisphere equal area stereograms showing foliation and lineation trends in the field area. Black planes represent average foliation plane. Stretching lineations are represented by dashed contoured lines. A) HSZ foliation and lineation relationships. B) SLSZ Bennet Ridgeline structural fabrics. C) SLSZ – Slide Lake cirque and Homestake ridgeline fabric relationships. From Lee et al. (2012).

Thin Section Data:

Sample	Locati	Latitude	Longitude	Strike	Dip	Trend	Plunge	Lithology	Mineral assemblage	Met. grade	Def. mech.	Def. T °C[1]	Shear sense	Vorticity	Monazite/Zircon
HS08-01	HC	39°29'16.4"	106°21'50.9"	26	75 SE	66	54	ultramylonite	qtz, fsp, chl, plag, musc, zr	chl	BLS-SGR	300-400	-	-	
HS08-02	HC	39°29'13.1"	106°21'46.6"	35	63 SE			granite	qtz, plag, ksp, musc, chl	chl	BLG	300	-	-	
HS08-03	HC	39°29'15.5"	106°21'49.6"	18	97 SE			ultramylonite	qtz, fsp, plag, musc, bt, op	bt	SGR	450-500	-	-	
HS08-04	HC	39°29'15.5"	106°21'49.6"	21	80 SE	95	97	quartz vein	qtz, little chl	chl	SGR	400-450	-	-	
HS08-05	HC	39°29'15.5"	106°21'49.6"	38	69 SE	105	68	ultramylonite	qtz, fsp, plag, bt, musc, chl	bt-chl	SGR	300-400	-	-	
HS08-06	HC	39°29'15.9"	106°21'41.5"	27	84 SE	114	68	ultramylonite	qtz, fsp, bt	bt	SGR	450-500	-	-	
HS08-07a/b	HCC	39°29'15.9"	106°31'49.5"	5	86 SE	114	85	mylonite	qtz, fsp, plag, sil, musc, bt	bt	SGR	450-500	t-NW	0.58-0.69	
HS08-08	HCC	39°29'15.9"	106°31'49.5"	19	83 SE	112	84	proto-mylonite	qtz, bt, plag, fsp, sil, musc,	sil-musc, (-chl)	SGR	400-500	t-NW	0.59-0.62	
HS08-09	HCC	39°29'15.9"	106°31'49.5"	342	90 SE	75	90	proto-mylonite	qtz, bt, plag, fsp, musc, chl	bt-chl	DLG-SGR	350-450	-	-	
HS08-10	HCC	39°29'15.9"	106°31'49.5"	30	83 SE	120	DD	mylonite	qtz, musc, bt, fsp, plag, mus	bt	SGR	450-500	-	0.58-0.70	
HS08-11	HCC	39°25'08.06	106°28'23.8"	21	DD	111	DD	proto-mylonite	qtz, musc, bt, fsp, plag, bt,	bt-chl	BLG-SGR	350-450	-	-	
HS08-12	HCC	39°25'08.06	106°28'23.8"	23	84 SE	113	DD	quartz vein	qtz, musc, fsp, ,bt	bt	SGR	450-500	t-NW	-	
HS08-13	HCC	39°25'08.06	106°28'23.8"	31	78 SE	121	DD	quartz vein	qtz, musc, fsp, ,bt	bt	SGR	450-500	t-NW	0.68-0.70	
HS08-14	HCC	39°25'08.06	106°28'23.8"	25	78 SE	115	DD	proto-mylonite	qtz, fsp, plag, musc, bt	bt	SGR	450-500	-	-	
HS08-15	HCC	39°25'08.06	106°28'23.8"	24	79 SE	114	DD	proto-mylonite	qtz, mic, plag, bt	bt	BLG-SGR	350-450	-	-	
HS08-16	HCC	39°25'08.06	106°28'23.8"	30	76 SE	120	DD	proto-mylonite	qtz, plag, bt, musc	bt	SGR	450-500	-	-	
HS08-17	HCC	39°25'06.0"	106°28'24.5"	16	69 NW	106	DD	bt gneiss	bt, qtz, fsp, musc	bt	BLG-SGR	300-500	-	-	
SL08-01	HP	39°22'00.5"	106°25'04.3"	2	69 SE	116	44	proto-mylonite	qtz, bt, plag, bt, chl	chl	BLG	300-400	t-NW	-	monazite - (1) centra
SL08-02	HP	39°22'01.5"	106°25'03.3"	10	42 SE	39	26	calc-sil marble	qtz, cal, chl	chl	BLG	300-400	t-SE	-	
SL08-03	HP	39°22'01.5"	106°25'03.1"	358	59 SE			calc mylonite	qtz, plag, chl	chl	BLG	300-400	-	-	
SL08-04	HP	39°22'01.5"	106°25'03.1"	2	65 SE			quartz vein	qtz, fsp, cal, epi, chl	chl	GBM	350-450	-	-	
SL08-05	HP	39°22'01.7"	106°25'02.6"	20	15 SE	13	6	marble lens	qtz, fsp, cal (no alignment)	bt	cal BLG (?)	400-450	-	-	
SL08-06	HP	39°22'01.5"	106°25'01.6"	59	6 NW	314	4	calc silicates	qtz, musc, qtz, cal, chl	chl	SGR	400-450	t-SE	-	
SL08-07	HP	39°22'01.5"	106°25'01.6"	330	21 NE	128	11	ultramylonite	qtz (GSR), bt, chl, musc	bt-chl	SGR	400-500	t-NE	-	monazite- (1) in alig
SL08-08	HP	39°22'01.5"	106°25'01.0"	332	26 NE	128	6	bt gneiss	qtz, bt, fsp,	bt	GBM	450-550	t-SW	-	
SL08-09	HP	39°22'01.5"	106°25'00.7"	341	29 NE	143	9	bt gneiss	qtz, bt, fsp, musc	bt	BLG	400-450	-	-	
HS09-01	HV	39.38619	106.45611	111	81SW	249	64	bt gneiss	qtz, mus, bt, plag, zr, fsp,	bt	BLG	400-450	-	-	
HS09-02	HV	39.38131	106.44994	101	89SW	295	59	bt gneiss	qtz, fsp, mus, bt (minor)	bt	BLG-SGR	400-500	-	-	
HS09-03	HCC	39.41398	106.48176	25	89SE	132	75	ultramylonite-b	qtz, bt (minor), fsp	bt	SGR	400-500	t-NW	-	
HS09-04	HCC	39.41408	106.48135	9	89NW	289	88	mylonite-bt	fsp, plag, qtz, bt, musc, chl	b-chl	BLG-SGR	300-450	-	-	
HS09-05	LL	39.37509	106.4289	295	84SW	20	73	bt gneiss	no thin section	-	-	-	-	-	
HS09-06	LL	39.37429	106.42839	229	74SE	40	80	mt	qtz, bt, chl, sil, fsp	sil-musc, bt-chl	GBAR	650+ (retro	350-400)	-	
HS09-07	LL	39.37174	106.42297	5	75SE			bt gneiss	qtz, bt, musc, ser	bt	GBAR	650+ (retro	-	-	
HS09-08	LL	39.37081	106.4229	353	76NE	178	78	calc-sil w/ bt	bt, cal, hbl, qtz	hbl-bt	GBAR	650+ (retro	-	-	
HS09-09	HV	39.39981	106.44854	115	84NW			gt/bt gneiss	bt, gt, sil, crd, qtz, kpar, mu	bt-gt-sil-crd	GBAR	600-700	-	-	monazite
HS09-10	HV	39.39981	106.44854	281	80SW			gt/bt/sil gneiss	bt, gt, sil, crd, qtz, kpar, mu	bt-gt-sil-crd	GBAR	600-700	-	-	monazite
HS09-11	BC	39.39777	106.38004	30	17SE	212	30	bt gneiss	qtz, fsp, sil, bt, chl, mus (op	sil-musc, bt-chl	GBAR	650+ (retro	-	-	
HS09-12	BC	39.3903	106.38653	41	78SE	41	46	marble	cal, amp? (minor qtz)	chl-bt	P sol'n	350-400	-	-	
HS09-13	BC	39.38668	106.39079	32	47SE	121	41	bt schist, mayb	qtz, bt, gt, chl, rt, zr, musc	bt, gt-chl	GBAR	~500-600 re	-	-	zircon in garnets
HS09-14	BC	39.3838	106.39273	41	43SE	66	21	bt gneiss	qtz, fsp, bt, plag,	bt	BLG	350-450	-	-	
HS09-15	BC	39.38285	106.39455	55	16NW	287	17	mt	qtz, bt, fsp, mus	bt	BLG	350-450	-	-	
HS09-16	BC	39.38233	106.39613	140	9NW	159	7	bt schist	qtz, bt, fsp	bt	BLG	350-450	-	-	
HS09-17	BC	39.38872	106.38979	38	90	163	75	proto-mylonite	qtz, chl, musc	chl	BLG	300-350	-	-	
HS09-18	Hwy 2	39.42691	106.3217	56	83NW	45	76	quartzite	qtz, fsp, bt	bt	GBAR	650+ (retro	-	-	
HS09-19	BC	39.38128	106.39923	150	24NE	118	21	bt gneiss	qtz, zr, rt, mus, bt, fsp	bt	GBAR	650+ (retro	-	-	
HS09-20	BC	39.38274	106.39385	74	56NW	57	25	bt gneiss	qtz, zr, rt, mus, bt, fsp, plag	plag-musc	GBAR	650+	-	-	
HS09-21	SLC	39.37578	106.39728	120	16NE	320	7	mylonite	qtz, fsp, bt, epi, zr	bt	BLG	350-450	-	-	

HS09-22	SLC	39.37578	106.39728	50	14NW	324	6	mylonite	qtz, sil, mus, bt,	sil-to-musc	high T overprinted by BI	t-SE	-			
HS09-23	SLC	39.37578	106.39728	123	7NE	324	6	mylonite	qtz, musc, bt, sil	bt-sil to musc	GBAR	650+ (retro	t-SE	-		
HS09-24	SLC	39.37578	106.39728	95	19NE	324	19	mylonite	qtz, fsp, sil, bt, musc, ap,	bt, sil to musc,	GBM to GB	650+ (retro	t-SE	-	monazites - (1) g	
HS09-25	SLC	39.37578	106.39728	20	27SE	145	12	mylonite	qtz, cal, musc, bt, rt, minor	bt minor sil	GBM	650+ (retro	t-SE	-		
HS09-26	SLC	39.37712	10639927	62	12NW	351	9	calc-sil mylonit	qtz, hbl, bt, cal, sphene	bt	SGR-GBM	450-600	t-SE	-		
HS09-27	SLC	39.37421	106.39898	148	21NE	144	2	mylonite	qtz, bt, musc, fsp, chl	bt, chl	GBAR	650+ (retro	t-SE	-		
HS09-28	SLC	39.37632	106.4044	53	24SE	152	23	mylonite	qtz, musc, bt	bt	GBM	500-600	t-SE	-		
HS09-29	SLC	39.37183	106.4027	65	43NW	312	41	migmatite	qtz, bt, musc, sil, rt	sil-musc, bt	GBAR	650+ (retro	t-NW	-		
HS09-30	SLC	39.37161	106.40327	80	6SE	134	4	mylonite	qtz, bt, musc, sil, rt, sil	sil-musc, bt	GBM	500-600	t-SE	-		
HS09-31	SLC	39.38977	106.41329	20	13SE	150	9	calc-mylonite	qtz, musc, bt, minor hbl, sil	bt-sil to musc	GBM	500-650	t-SE	-		
HS09-32	SLC	39.3711	106.41167	165	17NE	345	17	mylonite	qtz, musc, bt, mag, chr, sil	bt-sil to musc	GBM	500-650	t-NW	-		
HS09-33	SLC	39.37324	106.40826	155	10NE	123	6	mylonite	qtz, bt, musc, sil, opq,	bt-sil to musc	(earlier high	650+	t-SE	-		
HS09-34	SLC	39.37324	106.40826	156	27NE	332	6	mylonite	qtz, fsp, bt, chl	chl	GBAR	650+ (retro	t-SE	-		
HS09-35	SLC	39.37583	106.40716	102	22NE	299	4	my?	qtz, sil, musc,	bt, sil to musc	GBM	450-650	t-SE	-		
HS09-36	SLC	39.37876	106.40499	139	28NE	8	23	my?	qtz, bt, musc, fsp, bt	bt	high T overp	650 overprii	t-NW	-	monazite - (1) m	
HS09-37	SLC (	39.37971	106.40302	161	46NE	347	38	? mylonite	qtz, fsp, bt, musc, chl (lots!	chl	BLG	300-400	t-NW	-		
HS09-38	SLC	39.22265	106.24702	133	21NE	357	12	mylonite	qtz-fsp (dom.)musc, bt, sil	bt	GBAR	650+ (retro	t-NW	-		
HS09-39	SLC	39.37517	106.39431	35	13NW	325	13	mylonite	qtz, musc, bt, minor chl	bt	BLG	450-500	t-SE	-		
HS09-40	SLC	39.37509	106.39489	57	28NW			mylonite	qtz, fsp, bt, musc, sil, ap, ch	chl, sil-to-musc	BLG	450-500	t-S	-		
HS09-41	SLC	39.37509	106.39489	70	37NW	4	41	mylonite	qtz, bt, musc, sil	bt, sil to musc	GBAR	650+ (retro	-	-		
HS09-42 a/b	BR	39.37498	106.39156	51	68SE	164	65	mylonite	qtz, fsp, bt, mus, zr,	bt	GBM	450-600	t-SE	0.72-0.79	big zr in the fabr	
HS09-43	BR	39.37378	106.39246	51	70SE	175	54	mylonite	qtz, musc, bt, fsp, zr	bt	GBM	450-600	t-SE	0.71-0.72		
HS09-44 a/b	BR	39.37378	106.39246	35	67SE	170	69	mylonite	qtz, fsp, musc, bt, zr, sphen	bt	GBM	450-600	t-SE	0.70-0.72		
HS09-45	BR	39.37378	106.39246	225	75SE	170	64	mylonite	qtz, fsp, zr, musc	bt	GBM	450-600	t-SE	0.68-0.73	monazite - (1) all	
HS09-46	BR	39.37378	106.39246	50	50SE	170	44	mylonite	qtz, fsp, zr, musc, cr, bt	bt	GBM	450-600	t-SE	0.63-0.65	zircon	
HS09-47	BR	39.3749	106.39115	39	73SE	189	59	mylonite	qtz, fsp, bt, chl, zr	chl-bt	SGR-GBM	400-600	t-SE	0.58-0.65	monazite	
HS09-48	BR	39.37488	106.39124	42	69SE	76	61	mylonite	qtz, bt, musc, fsp	bt	BLG-SGR	350-450	-	-		
HS09-49	BR	39.37488	106.39124	48	63SE	70	44	mylonitized qtz	qtz, fsp, bt, musc	bt	SGR-GBM	450-550	-	-		
HS09-50	BR	39.37488	106.39124	75	88SE	191	86	mylonite	qtz, bt, fsp, zr, minor chl	bt	BLG-SGR	350-450	-	-	monazite - (1) m	
HS09-51	BR	39.369	106.40208	108	44SW	170	41	mylonite	qtz, bt, fsp	bt	GBM	450-600	t-NW	-		
HS09-52	BR	39.37775	106.3879	65	72SE	212	61	calc-sil mylonit	qtz, chl, bt, musc, cal	chl-bt	GBAR	650+ (retro	t-SE	-		
HS09-53	BR	39.37967	106.39461	76	61SE	194	59	qtz-feld gneiss	qtz, fsp, zr, chl, gt, sil	chl-bt-gt-sil	GBAR	650+ (retro	-	-		
HS09-54	SLC	39.36621	106.41617	36	28SE	155	28	mylonite	qtz, fsp, musc, bt	bt	BLG	350-400	t-SE	-		
HS09-55	SLC	39.36119	106.41799	144	44NE	351	26	mylonite	qtz, fsp, bt, sil, musc	sil-to-musc, bt	GBAR	650+ (retro	-	-		
CC08-01	GGSP	39°51'06.8"	105°23'00.7"	29	vertical	weak	0	basal quartzite	qtz, op, sil, bt	sil	BLG-SGR	250-400	-	-		
CC08-02	GGSP	39°51'38.7"	105°21'26.1"	185	52SE	151	38	mylonite	qtz, fsp, bt, ms, ms, ser	bt	BLG	<250	t-NW	-		
CC08-03	GGSP	39°51'38.7"	105°21'26.1"	190	54SE	334	36	mylonite	qtz, fsp, plag, ms, bt, ser	bt	BLG	<250	t-SE	-		
CC08-04	GGSP	39°51'37.4"	105°21'29.1"	206	51SE	162	38	ultramylonite	qtz (micro), ksp, op	bt	BLG	<250	t-NW	-		
CC08-05	GGSP	39°51'35.4"	105°21'31.3"	50	86SE	154	81	quartz vein	qtz, ms, bt, ksp	bt	BLG	<250	t-SE (lt. m f	-		
CCO8-06	GGSP	39°51'35.4"	105°21'31.3"	228	84SE	down dip		quartzite	qtz, ms, bt, zr, op,	bt	BLG+	250-300	t-NW (ogsf)	-		
CC08-07	GGSP	39°51'35.2"	105°21'31.3"	214	85SE	121	74	quartzite	MIA	-	-	-	-	-		
CC08-08	GGSP	39°51'28.56	105°21'30.69	221	74SE	down dip		quarzite	qtz, ms, op	chl	BLG	<250	-	-		

Location abbreviations: (HC) Hornsilver campground, (HCC) Holy Cross City, (HP) Homestake Peak, (LL) Lost Lakes, (HV) Homestake Valley, (BC) Bennett Cirque, (SLC) Slide Lake Cirque, (BR) Bennett Ridgeline, (GGSP) Golden Gate State Park.

Mineral abbreviations: (qtz) quartz, (bt) biotite, (fsp) feldspar, (musc) muscovite, (chl) chlorite, (sil) sillimanite, (zr) zircon, (cal) calcite, (gt) garnet, (crd) cordierite, (ap) apatite, (hbl) hornblende, (rt) rutile, (plag) plagioclase

Deformation temperatures: derived from quartz and feldspar texures from Stipp et al., 20002 (qtz) and Pryer, 1993 (fsp), and Spear (1993)

Shear sense: from oriented samples, indicators include: mica fish, rigid tails on porphyroclasts, oblique grain shape fabric, shear bands…

Vorticity: Mean kinematic vorticity (Wm) derived from the Rigid Grain Net technique (see text for methodology)

[1]Deformation temperatures derived from quartz textures (Stipp et al., 2002a,b) feldspar textures from (Pryer, 1993), metamorphic mineral assemblage (Spear, , and quartz LPOs

VITA

Carsen Adams grew up in Rockingham, North Carolina. Carsen attended Richmond Early College Highschool where he was able to earn an associate degree while earning his high school diploma. After finishing high school, he attended the University of North Carolina at Charlotte and received a Bachelor of Science degree in Geology in 2020, earning the "Outstanding Senior in Geology" award. While at UNC Charlotte, Carsen completed an independent study focused on developing methods to quantify subcritical cracking in rocks from Antarctica. In 2019, he attended the North Carolina geologic field course offered by East Carolina University, an adventure that solidified his love for geology. He began a Master of Science in Geology at the University of Tennessee Knoxville's Department of Earth and Planetary Sciences in August of 2020. While at UTK, Carsen was advised by Dr. Micah Jessup while studying the kinematics of shear zones within the Colorado Mineral Belt and presented his research at AGU 2021 in New Orleans. He spent a week in Leadville, CO completing field work for his thesis in the summer of 2021. Additionally, Carsen enjoyed teaching undergraduate introductory geology lab and the upper division structural geology lab.